Synthetic Dioxygen-carrying Hemoprotein. Human Serum Albumin Including Iron(II) Complex of Protoporphyrin IX with an Axially Coordinated Histidylglycyl-propionate

Akito Nakagawa, Teruyuki Komatsu, Naomi Ohmichi, and Eishun Tsuchida*
Advanced Research Institute for Science and Engineering, Waseda University, 3-4-1 Okubo Shinjuku-ku, Tokyo 169-8555

(Received February 28, 2003; CL-030171)

Human serum albumin incorporating the iron(II) complex of protoporphyrin IX having an axially coordinated histidylglycyl-propionate formed a dioxygen-adduct complex in aqueous media (pH 7.3). The O_2-binding affinity ($P_{1/2}$) was 0.1 Torr at 25 °C.

Apomyoglobin spontaneously incorporates an iron(III) complex of protoporphyrin IX (hemin) and enable the prosthetic group to bind a dioxygen molecule (O_2).[1,2] Human serum albumin (HSA), the most abundant plasma protein in our blood stream, also captures a hemin dissociated from methemoglobin and accommodates it in the subdomain IB.[3,4] However, this HSA-hemin hybrid cannot form the O_2-adduct complex, even if one reduces the central ferric ion of the hemin to the ferrous state. We have shown that HSA including highly encumbered tetraphenylporphinato-iron(II) (Fe^{2+}TPP) derivatives can only bind and release O_2 under physiological conditions similar to hemoglobin (Hb) and myoglobin (Mb).[5] The prerequisites of these stable dioxygenations were believed to provide the Fe^{2+}TPP structure with (i) steric hindrance around the O_2-binding site to prevent proton access, and (ii) a covalently bound proximal imidazole. More recently, we have found that the iron(II) complex of protoporphyrin IX having an axially coordinated histidylglycyl-propionate is also included into the HSA interior and forms an O_2-adduct in aqueous media at 25 °C. This communication reports for the first time the HSA hybrids incorporating natural protoheme IX derivatives as novel synthetic O_2-carrying hemoproteins.

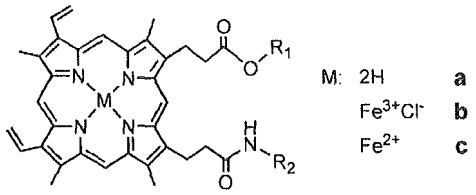

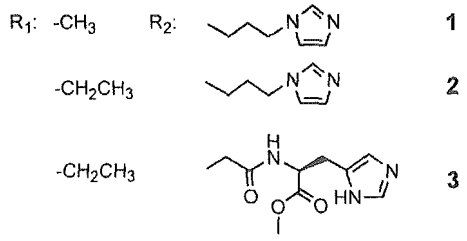

The free-base porphyrin of the pioneering Mb model, chelated heme **1a**,[6] was synthesized by our one-pot reaction procedure using benzotriazol-1-yloxytris(dimethylamino)phosphonium hexafluorophosphate (BOP) at room temperature in pyridine. After the reaction, the mixture, when poured into excess water, led to precipitation of the crude product; the pyridine, water soluble BOP, and formed hexamethylphosphoramide were easily filtered off. Compound **2a** with an ethyl propionate, and compound **3a** having a histidylglycyl-propionate were also prepared in the same manner (Yield: 30%).[7] The iron insertion was performed using $FeCl_2$ in DMF to give the corresponding hemin derivatives. The analytical data of all compounds were satisfactorily obtained.[8]

The UV–vis absorption spectrum of the ferrous complex **3c** (λ_{max}: 423, 533, 555 nm) in DMF showed the formation of the typical five-*N*-coordinated high-spin iron(II) complex as well as **1c** and **2c**. Upon the bubbling of O_2 gas through this solution, the UV–vis absorption immediately changed to that of the O_2-adduct complex (λ_{max}: 408, 540, 575 nm). The dioxygenated **3c** transferred to the stable carbonyl species (λ_{max}: 419, 537, 568 nm) after the exposure of carbon monoxide (CO). The O_2-binding affinity ($P_{1/2}$) of **3c** was determined to be 0.2 Torr in DMF solution, which is slightly lower (high affinity) than those of **1c** and **2c** ($P_{1/2}$: 0.3 Torr) (Table 1).[6d] The O_2-binding affinity normally elevates in proportion to an increase in the basicity of the trans-coordinated imidazole,[9] but histidine in **3c** showed a smaller pK_a (6.0) in comparison to the value of 1-(acetoamidopropyl)imidazole (pK_a = 6.6) for **2c**. The high O_2-binding affinity of **3c** is presumably due to a favorable geometry of the imidazole bonding to the central iron, which was supported by the preliminary results on our molecular simulations of the dioxygenated **3c** complex.[10]

The hybridization of HSA and the protoheme IX derivatives (molar ratio: 1/1) were carried out as follows. The ethanol solution of the carbonylated heme (1.6 mM, 50 μL) was slowly injected into the phosphate buffered solution (pH 7.3, 1 mM) of the recombinant HSA (rHSA)[11] (20 μM, 4 mL) under an argon atmosphere. The obtained aqueous solutions were stable for a few months without precipitation. The UV–vis absorption spectra of the rHSA-heme hybrids showed formation of the CO-ad-

Table 1. O_2-binding parameters of rHSA-protoheme IX derivatives at 25 °C

	pK_a	$P_{1/2}$ (Torr)		$\tau_{1/2}$ (min)
		in DMF	rHSA hybrid in water	rHSA hybrid in water
1c	6.6[a]	0.3	0.1	20
		0.3[b]	1.0[c]	—
2c	6.6[a]	0.3	0.1	50
3c	6.0[d]	0.2	0.1	90

[a]p*Ka* value of 1-(acetoamidoprpoyl)imidazole in water (Ref. 6b), [b]Ref. 6d, [c]2% Aqueous myristyltrimethylammonium-bromide suspension (Ref. 6c). [d]p*Ka* value of histidine in water.

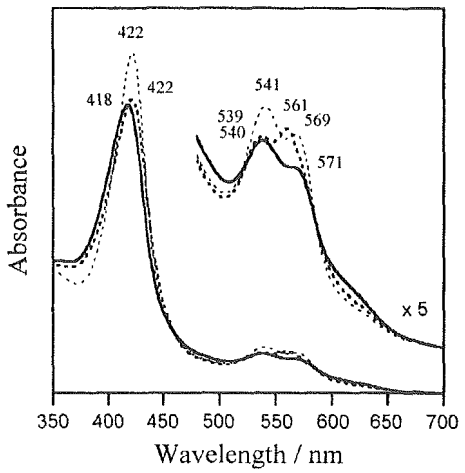

Figure 1. UV–vis absorption spectral changes of rHSA-**3c** in phosphate buffered solution (pH 7.3, 25 °C); under Ar: ----, under O_2: —, under CO: ·····.

duct complexes (Figure 1). The binding number of protoheme IX derivative in one albumin molecule was confirmed to be one by assay of the each concentration and the relatively high binding constants of the hemes for rHSA (K_1: ca. 4×10^6 M^{-1}). The isoelectric points ($pI = 4.8$) and circular dichloism spectra of rHSA-hemes were identical to those observed for rHSA itself, which indicated that the surface net charges and second-order structure of rHSA host did not change after incorporation of the heme guest. Light irradiation of the carbonyl complex of rHSA–**3c** led to CO dissociation and a changing of spectrum, in which two peaks appeared in the Q band region; the resulting spectral shape resembles that of the six-coordinated low-spin mesoheme derivatives.[6b] This result implies that the sixth coordination site of **3c** is occupied by some amino acid residue of albumin. The spectral feature of rHSA–**1c** and rHSA–**2c** also showed the same trend.

Upon exposure of the rHSA–**3c** solution to O_2, the UV–vis absorption spectrum rapidly changed to that of the O_2-adduct complex (Figure 1). From the recent result on our crystal structural analysis of rHSA-hemin hybrid,[4] we infer that the protoheme derivatives **1c**, **2c**, and **3c** are also accommodated into the hydrophobic site of the subdomain IB, and it may contribute to their O_2-adduct complex formation. The O_2-binding affinity ($P_{1/2}$) of rHSA–**2c** and rHSA–**3c** were determined to be both 0.1 Torr. Accompanying the autooxidation of the central iron(II), the absorption band (λ_{max}: 540, 571 nm) slowly decreased, leading to the formation of the inactive protohemin. The half life-times ($\tau_{1/2}$) of the O_2-adduct species for rHSA–**2c** and rHSA–**3c** were 50 min and 90 min, respectively (Table 1). We concluded that the axially bound histydylglycyl-propionate to protoheme IX provided a more stable O_2-adduct compared to the imidazolyl one, and the ethyl propionate on the other side also contributed the increased stability for the dioxygenated complex relative to the methyl-propionate ($\tau_{1/2}$ of rHSA–**1c**: 20 min).

In conclusion, rHSA successfully incorporated protoheme IX derivatives with an intramolecularly coordinated proximal base, giving rHSA-heme hybrids, which form O_2 adducts at 25 °C. These are the first examples of the synthetic O_2-carrying hemoproteins containing the natural protoheme IX derivative as a prosthetic group, which may also act as a very new class of artificial hemoprotein enzymes as well.

This work was partially supported by Health Science Research Grants (Research on Pharmaceutical and Medical Safety) of the MHLW, and by a Grant-in-Aid for Scientific Research (No. 13650938) from the MEXT.

References and Notes

1 T. Hayashi, H. Dejima, T. Matsuo, H. Sano, D. Murata, and Y. Hisaeda, *J. Am. Chem. Soc.*, **124**, 11226 (2002).
2 S. Neya, K. Imai, H. Hori, H. Ishikawa, K. Ishimori, D. Okuno, S. Nakatomo, T. Hoshino, M. Hata, and N. Funasaki, *Inorg. Chem.*, **42**, 1456 (2003).
3 M. Wardell, Z. Wang, J. X. Ho, J. Robert, F. Ruker, J. Ruble, and D. C. Carter, *Biochem. Biophys. Res. Commun.*, **291**, 813 (2002).
4 P. A. Zunszain, J. Ghuman, T. Komatsu, E. Tsuchida, and S. Curry, "Protein Data Bank." code: 1O9X, paper in preparation.
5 a) T. Komatsu, K. Ando, N. Kawai, H. Nishide, and E. Tsuchida, *Chem. Lett.*, **1995**, 813. b) T. Komatsu, K. Hamamatsu, J. Wu, and E. Tsuchida, *Bioconjugate Chem.*, **10**, 82 (1999). c) E. Tsuchida, T. Komatsu, Y. Matsukawa, K. Hamamatsu, and J. Wu, *Bioconjugate Chem.*, **10**, 797 (1999). d) T. Komatsu, T. Okada, M. Moritake, and E. Tsuchida, *Bull. Chem. Soc. Jpn.*, **74**, 1695 (2001). e) T. Komatsu, Y. Matsukawa, and E. Tsuchida, *Bioconjugate Chem.*, **13**, 397 (2002).
6 a) W. S. Brinigar, C. K. Chang, J. Geibel, and T. G. Traylor, *J. Am. Chem. Soc.*, **96**, 5597 (1974). b) J. Geibel, J. Cannon, D. Chambell, and T. G. Traylor, *J. Am. Chem. Soc.*, **100**, 3575 (1978). c) T. G. Traylor, C. K. Chang, J. Geibel, A. Berzinis, T. Mincey, and J. Cannon, *J. Am. Chem. Soc.*, **101**, 6716 (1979). d) T. G. Traylor and P. S. Traulor, *Annu. Rev. Biophys. Bioeng.*, **11**, 105 (1982).
7 Glycyl-L-histidine methyl ester dihydrochloride was prepared according to the previously reported procedures [E. Monzani, L. Linati, L. Casella, L. D. Gioia, M. Favretto, M. Gullotti, and F. Chillemi, *Inorg. Chim. Acta*, **273**, 339 (1998)].
8 Spectoscopic data: **2a**; ^{1}H-NMR (500 MHz, $CDCl_3$) δ −3.6 (s, 2H, inner-H), 0.9 (t, -COO-CH_2CH_3, 3H), 1.1–1.5 (m, 2H, -CH_2CH_2-imidazole (Im)), 2.9–3.1 (m, -C(=O)NH-CH_2CH_2-, 2H), 3.1–3.3 (m, -CH_2CH_2COO-, 4H), 3.4–3.7 (m, porphyrin (por.)-CH_3, -CH_2CH_2-Im, 14H), 3.7–3.9 (m, -COO-CH_2CH_3, 2H), 4.1–4.4 (m, por.-CH_2-, 4H), 5.9–6.4 (m, vinyl =CH_2, Im, 5H), 6.6 (d, Im , 1H), 6.9 (s, Im , 1H), 8.1–8.3 (m, vinyl-CH=, 2H), 9.8–10.1 (m, *meso*, 4H). FAB-MS (*m/z*): 698.4 [M-H^+]. IR (cm^{-1}): 1650 ($\nu_{C=O}$ (amido)), 1732 ($\nu_{C=O}$ (ester)). UV–vis ($CHCl_3$) λ_{max}: 409, 509, 544, 580, 633 nm. **2b**; FAB-MS (*m/z*): 752.4 [M-Cl^-]. IR (cm^{-1}): 1651 ($\nu_{C=O}$ (amido)), 1725 ($\nu_{C=O}$ (ester)). UV–vis ($CHCl_3$) λ_{max}: 406, 520, 578 nm. **3a**; ^{1}H-NMR (500 MHz, $CDCl_3$) δ −4.6 (s, 2H, inner-H), 2.7–2.9 (m, Im-CH_2-, 2H), 3.0–3.5 (m, por.-CH_3, -CH_2CH_2CONH-, -CH_2 CH_2-COO-CH_2CH_3, 18H), 3.6 (s, -CONH-CH_2CONH-, 2H), 4.0–4.3 (d, por.-CH_2, 4H), 4.3–4.5 (m, α-CH, 1H), 6.0–6.4 (m, vinyl =CH_2, 4H), 7.4 (s, Im , 1H), 8.0–8.3 (m, vinyl-CH=, Im, 5H), 9.8–10.0 (m, *meso*, 4H). FAB-MS (*m/z*): 785.4 [M-H^+]. IR (cm $^{-1}$): 1635 ($\nu_{C=O}$ (amido)). 1725 ($\nu_{C=O}$ (ester)). UV–vis ($CHCl_3$) λ_{max}: 405, 505, 541, 577, 627 nm. **3b**; FAB-MS (*m/z*): 838.4 [M-Cl^-]. IR(cm^{-1}): 1660 ($\nu_{C=O}$ (amido)), 1734 ($\nu_{C=O}$ (ester)). UV–vis ($CHCl_3$) λ_{max}: 388, 508, 637 nm.
9 D. V. Stynes, H. C. Stynes, B. R. James, and J. A. Ibers, *J. Am. Chem. Soc.*, **95**, 1796 (1973).
10 The esff forcefield simulation was performed using an Insight II system (Molecular Simulation Inc.). The structure was generated by alternative minimization and annealing dynamic calculation.
11 A. Sumi, W. Ohtani, K. Kobayashi, T. Ohmura, K. Tokoyama, M. Nishida, and T. Suyama, "Biotechnology of Blood Proteins." John Libbey Eurotext, Montrouge (1993), Vol. 227, p 293.

Published on the web (Advance View) May 13, 2003; DOI 10.1246/cl.2003.504

Molecular Energy and Electron Transfer Assemblies Made of Self-Organized Lipid-Porphyrin Bilayer Vesicles

Teruyuki Komatsu, Miho Moritake, and Eishun Tsuchida*[a]

Abstract: Novel molecular energy and electron transfer assemblies in vesicular form, which are made of self-organized amphiphilic porphyrins bearing phospholipid-like substituents (lipid-porphyrins), have been photochemically characterized. Tetraphenylporphyrin (TPP) derivatives with four dialkylphosphocholine groups [free-base (**1a**), Zn^{2+} complex (**1b**), and Fe^{3+} complex (**1c**)] are spontaneously associated in water to form spherical unilamellar vesicles with a diameter of 100–150 nm. Exciton calculations based on the bilayered sheet model of **1b**, which has a porphyrin packing similar to that seen in the triclinic unit cell of the Zn^{2+}TPP crystals, reproduced the Soret band bathochromic shift appearing in the aqueous solution of **1b** well. The UV/Vis absorption spectrum of the **1a/1b** hybrid vesicles (molar ratio: 1/1) showed no electronic interaction between the two porphyrin chromophores in the ground state, but efficient intermolecular singlet–singlet energy transfer took place from the excited **1b** donors to the **1a** acceptor within the vesicle. Near-field scanning optical microspectroscopy of the **1a/1b** vesicles on a graphite surface also showed only free-base porphyrin fluorescence. The efficiency of the energy transfer was 0.81 and the rate constant was $3.1 \times 10^9\ s^{-1}$. On the other hand, protoporphyrin IX bearing two alkylphosphocholine propionates (**2**) was incorporated into the **1a** or **1c** bilayer vesicles (ca. 100 nm ϕ, molar ratio: **1a/2** or **1c/2** = 10). The UV/Vis absorption spectrum showed that **2** was successfully anchored into the fluid alkylene region of the membrane without stacking. Photoirradiation (λ_{ex}: 390 nm) of the **1c/2** vesicles in the presence of triethanolamine led a vectorial electron transfer from the outer aqueous phase to the membrane center, which allowed reduction of the ferric ion of the Fe^{3+}TPP platform.

Keywords: electron transfer · energy transfer · porphyrinoids · self-assembly · vesicles

Introduction

In nature, solar energy conversion is triggered by the capturing of sunlight by hundreds of chlorophyll arrays. That excited energy is funneled to a reaction center by an extremely efficient transfer of energy and is converted to chemical potential in the form of a long-lived charge-separated state.[1] To obtain insight into these natural light-harvesting events, numerous porphyrinoid arrays linked by covalent bonds have been synthesized.[2, 3] Nonetheless, general organic synthetic procedures did not allow the construction of a large-scale supramolecular architecture in which more than hundreds of metalloporphyrins are ordered with great regularity. Thus, noncovalent approaches could present considerable advantages.[4, 5] Furthermore, if we are to reproduce any biochemical reaction, the aqueous medium is particularly important. From these points of view, self-organized porphyrin assemblies have attracted attention as a potential light-harvesting antennae model in water. Whereas porphyrin H-aggregates are generally quenched due to the large exciton couplings,[6] J-aggregated porphyrins show strong fluorescence.[7] One of the most significant examples of the emitting assemblies is our spherical bilayered vesicles made of amphiphilic tetraphenylporphyrin (TPP) with four phospholipid-like substituents (lipid-porphyrin, **1a**); its fluo-

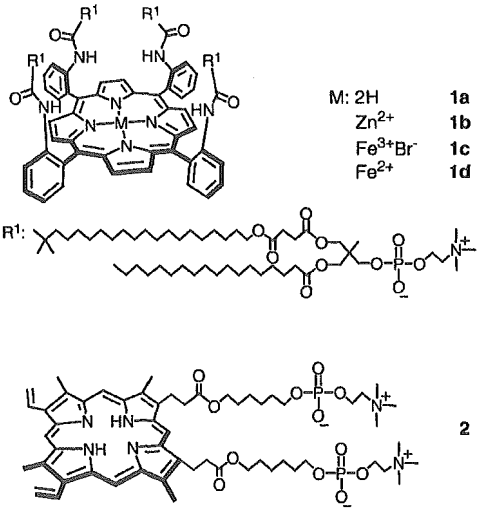

[a] Prof. E. Tsuchida, Dr. T. Komatsu, M. Moritake
Advanced Research Institute for Science and Engineering Waseda University, Tokyo 169-8555 (Japan)
Fax: (+81) 3-3205-4740
E-mail: cishun@waseda.jp

DOI: 10.1002/chem.200305013

rescence intensity remained 76% of that of the monomer in organic solvent.[8] Herein, we report on novel bilayer vesicles consisting of two lipid-porphyrin ensembles [free-base (**1a**) and Zn^{2+} complex (**1b**)], in which an efficient singlet–singlet energy transfer took place based on the in-plane tightest packing of the porphyrin platforms. In addition, we present vectorial electron migration from the bulk aqueous phase to the membrane center of the Fe^{3+} complex lipid–porphyrin (**1c**) vesicles. The amphiphilic protoporphyrin IX (**2**) anchored into the highly oriented alkylchain region acts as an electron transfer mediator. Photoirradiation (λ_{ex}: 390 nm) under the coexistence of triethanolamine allowed reduction of the central ferric ions of the Fe^{3+} porphyrins and gave an O_2-coordinating ability to the vesicles.

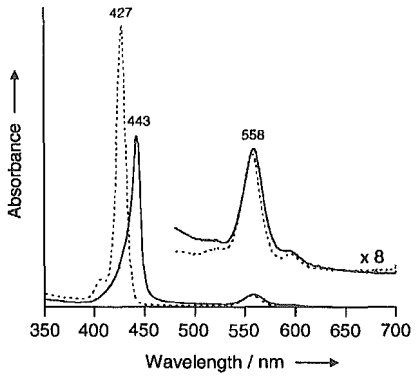

Figure 2. UV/Vis absorption spectra of **1b** at 25 °C: a) in benzene/MeOH (4:1 v/v) (dotted line) and b) in water (solid line).

Results and Discussion

Nanostructure and fluorescence of the lipid-porphyrin vesicles: The newly synthesized Zn^{2+} complex of lipid-porphyrin **1b** was dispersed in deionized water by ultrasonication to give a pink-colored colloidal solution. Transmission electron microscopy (TEM) of the negatively stained and evaporated sample on a copper grid showed that **1b** forms spherical unilamellar vesicles with a diameter of 100–150 nm as well as the corresponding free-base porphyrin **1a** and the Fe^{3+} complex **1c** (Figure 1a).[8c] The thickness of the membrane

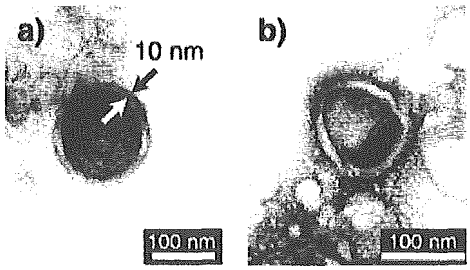

Figure 1. Transmission electron micrographs of evaporated aqueous solutions of a) **1b** and b) **1a**/**1b** ensemble (molar ratio: 1/1). The samples were negatively stained by uranylacetate.

was 10 nm, which is twice the molecular length of **1b** (4.6 nm). Most probably, the hydrophobic Zn^{2+}TPP platforms were arranged in two-dimensional planar sheets, which were stacked with a lateral displacement at the center of the membrane. It could be an identical conformation to that seen in the **1a** vesicles.[8c] The huge lipid-porphyrins (molecular weight over 4500) cannot produce a large curvature, so that they form giant unilamellar vesicles. This is in contrast to the fact that the usual phospholipids form small unilamellar vesicles (30–40 nm ϕ) by the same preparation.

The UV/Vis absorption spectrum of the aqueous solution of **1b** showed a porphyrin Soret band at 443 nm (ε_{max}: $2.7 \times 10^5\ M^{-1}cm^{-1}$), and its maximum was red shifted (+16 nm) compared to that of the monomer in benzene/MeOH (4:1 v/v) solution (λ_{max}: 427 nm) (Figure 2). On the contrary, the porphyrin Q bands remained essentially unaltered (only a 1 nm red shift). This larger bathochromic shift of the Soret band should include excitonic interactions due to a lateral arrangement (J-aggregate) of the transition moments of the porphyrin chromophores.

We then did a quantitative analysis of the excitonic interactions of the bilayered Zn^{2+} porphyrin sheets according to our previously reported procedure.[8c] The simple point-dipole exciton coupling theory was employed,[9] and two hypotheses were postulated: 1) the tightest packing of the Zn^{2+}TPP moieties is realized within a rhomboidal lattice, which is observed in the triclinic unit cell of the single crystal of the unsolvated Zn^{2+}TPP (Figure 3, 2*a*: 2.6 nm, 2*b*: 1.48 nm),[10] and 2) the interlayer (*d*) of the face-to-face

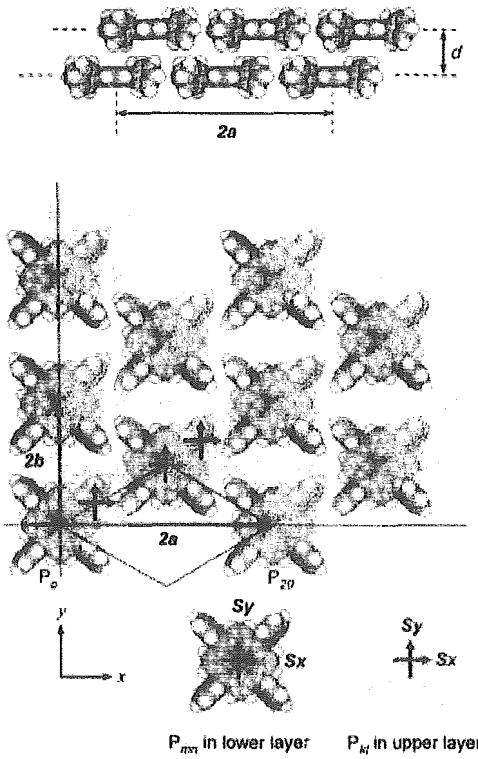

Figure 3. Predicted arrangements of the Zn^{2+}TPP platforms as a model for the bilayer membrane of **1b**. The porphyrin P_o is located at the origin of the coordinate axes.

stacking of the porphyrin sheets is 6.0 Å (Figure 3). The exciton interaction (ΔE) between the two porphyrins in the monolayer is given by Kasha's Equation (1).

$$\Delta E = M^2 r_{mn}^{-3} (1 - 3\cos^2\theta) \quad (1)$$

M is the transition dipole moment of the Zn^{2+}TPP moiety in **1b** ($M^2 = 68.2\,D^2$),[11] r_{mn} is the center-to-center distance between the original porphyrin o (P_o) and the porphyrin mn (P_{mn}), and θ is the tilt angle between the line of centers and the molecular axes. Using the same strategy, we can estimate the exciton interactions between P_o and the porphyrin kl in the upper layer (P_{kl}).[12] These calculations eventually gave the total differences V and V' in two different Soret transitions S_x and S_y as -612.3 and $-239.0\ cm^{-1}$, respectively, that indicate split Soret peaks of 430.8 and 437.5 nm. The observed Soret band was definitely asymmetric, and it could be divided into two absorptions (438.5 and 441.4 nm). The small difference between the calculated λ_{max} and experimentally measured values is likely to be due to the van der Waals shift caused by the replacement of solvents. Thus, we can conclude that the absorption shift in the Soret band is describable by exciton interaction. Of course, the observed shift in the Soret band comes from the averaged interaction and involves some deviations, because of the fluidity of the membranes.

The most remarkable photophysical property of the lipid-porphyrin vesicles is their strong fluorescence in comparison to the other porphyrin aggregates.[6, 8c] The 3D excitation-emission spectrum of the aqueous **1b** solution showed that the fluorescence emission maxima (λ_{em}: 601, 653 nm) correlated with the absorption of the vesicles (λ_{max}: 443 nm) (not shown), which suggests that the fluorescence comes from the membrane and not the monomer dissociated from the aggregate. Single photon-counting fluorescence measurements were also done in air-equilibrated solution of **1b** vesicle. The fluorescence decay profile could be analyzed in terms of a single exponential process with a lifetime (τ_F) of 1.35 ns ($\kappa^2 = 1.14$), which was slightly shorter than the value of the **1b** monomer in benzene/MeOH (4:1 v/v) solution ($\tau_F = 2.0$ ns). The excited triplet states of the **1b** vesicles are too short to be observed by our nanosecond laser flash photolysis apparatus.

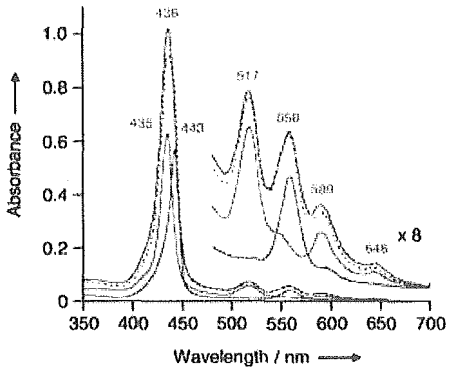

Figure 4. UV/Vis absorption spectra of **1a** vesicles (blue line), **1b** vesicles (red line), and **1a/1b** ensemble vesicles (molar ratio: 1/1, green line) in water at 25 °C. Black dotted lines represent the superposition of the spectra for **1a** and **1b**.

associated with the Zn^{2+} porphyrin and a corresponding increase in fluorescence associated with the free-base porphyrin (λ_{em}: 650, 712 nm) (Figure 5). Even on excitation at 558 nm, where the Zn^{2+} complex mainly absorbs (72 %), the emission spectral shape obviously demonstrated that of the

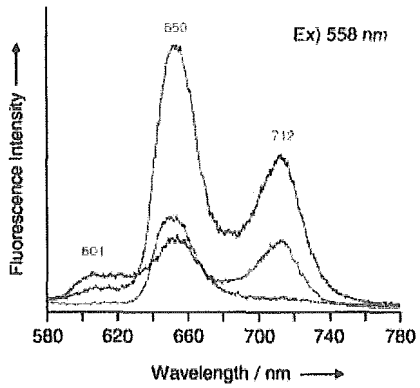

Figure 5. Steady-state fluorescence emission spectra of **1a** vesicles (blue line), **1b** vesicles (red line), and **1a/1b** ensemble vesicles (molar ratio: 1/1, green line) in water at 25 °C (Ex. 558 nm).

Energy transfer process within the lipid-porphyrin vesicles: Based on the exciton calculations, the alignment of the TPP planes in the free-base and the Zn^{2+} porphyrin vesicles would be identical. This result implies that they are able to produce homogeneous vesicular membranes. Indeed, the equivalent moles of **1a** and **1b** are spontaneously associated in water to yield spherical unilamellar vesicles with a diameter of 100–150 nm with a thickness of 10 nm (Figure 1b), in which the Zn^{2+} porphyrin should become the donor and the free-base porphyrin acts as the acceptor. The UV/Vis absorption spectrum of this **1a/1b** ensemble indicates that the spectral features are the sum of those from the individual lipid-porphyrin vesicles; it suggests no electronic interaction between **1a** and **1b** in the ground state (Figure 4). By contrast, its fluorescence spectrum is dramatically different from the superposition of those of the individual components. The **1a/1b** vesicles showed a decrease in fluorescence free-base porphyrin with stronger intensity by a factor of three. Because the fluorescence of the equivalent mixture of each vesicle solution displayed a simple sum of their spectra, efficient intermolecular singlet–singlet energy transfer could take place from the excited Zn^{2+} porphyrin donors to the statistically distributed free-base acceptor within the vesicles. Since the $\pi-\pi$ interactions between Zn porphyrins are usually somewhat stronger than those of the free-base porphyrins, there may not be a statistical dispersion of these two porphyrin chromospheres in the bilayer. However, for instance, the temperature dependence of the Soret band absorption maximum of the **1a/1b** vesicles showed a small hypsochromic shift at 56 °C, which suggests the gel-phase (liquid-crystal) transitions of the membrane. Very similar behavior was observed in the **1a** vesicles.[8a] This probably implied that the $\pi-\pi$ interactions between the Zn complexes are not so different from the free-bases in the lipid-porphyrin

vesicles. The fluorescence band of the donor considerably overlaps the acceptor absorption, therefore Förster-type excitation energy transfer would be preferable.[13]

The aqueous **1a/1b** vesicle solution was then transferred onto a graphite surface and subjected to near-field scanning optical microspectroscopy (NSOM). The bilayered membranes slowly flattened on the substrate during the water evaporation process. Unfortunately, the topology-mode measurements could not distinguish each 100 nm particle because of the low resolution. However, the dried vesicles still fluoresce on the solid surface and their emission was clearly detected by NSOM (Figure 6a). The fluorescence pattern of

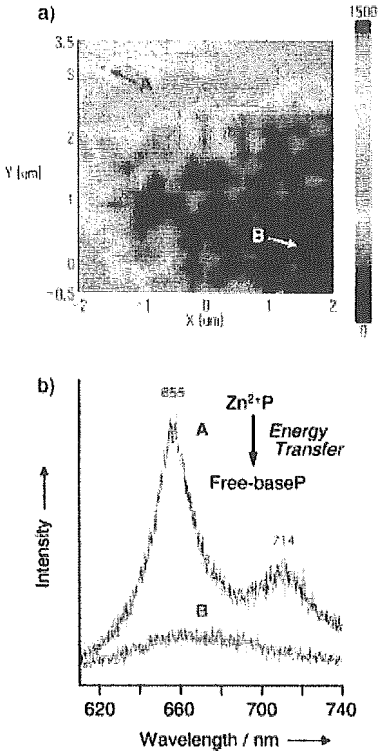

Figure 6. NSOM images of the evaporated aqueous solution of **1a/1b** ensemble vesicles (molar ratio: 1/1) on HOPG. a) fluorescence image of the flattened vesicles (4 × 4 μm, Ex. 442 nm, detection was effected at 650 nm), and b) fluorescence emission spectra of the flattened vesicles at the indicated parts [(A) and (B)] in the image a).

the collapsed **1a/1b** particles (λ_{em}: 655, 714 nm) was in good agreement with that of the free-base porphyrin [λ_{em}: 650, 712 nm, Figure 6b)]. Recently, Adams et al. reported interesting NSOM measurements of porphyrin thin films.[14] Our result is the first observation of an energy transfer molecular assembly made of amphiphilic porphyrin aggregates by the NSOM technique.

The fluorescence decay profile of this hybrid vesicle solution monitored at 610 nm became progressively triple-exponential with a faster decaying component being seen in addition to the original two slower kinetics ($\kappa^2 = 1.26$) (Figure 7). The longer lifetimes (6.73, 1.90 ns) are respectively assigned as those of **1a** and **1b**. The shorter-lived component (263 ps) is reflective of the singlet–singlet energy transfer

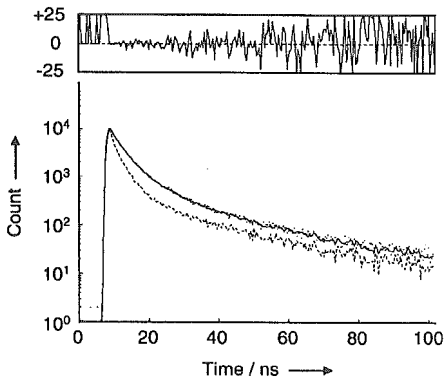

Figure 7. Time-correlated single-photon counting decay profile of **1a/1b** ensemble vesicles (molar ratio: 1/1, Ex. 558 nm, detection was effected at 610 nm). The curve is fitted to triple exponentials with lifetimes of 6.73 ns, 1.90 ns, and 263 ps ($\kappa^2 = 1.26$).

from the excited Zn^{2+} porphyrin to the free-base porphyrin within the vesicles. The rate constants for intermolecular energy transfer (k_{ET}) have been calculated from Equation (2).

$$k_{ET} = 1/\tau_{FB/Zn} - 1/\tau_{Zn} \quad (2)$$

$\tau_{FB/Zn}$ is the measured fastest component of the excited **1a/1b** vesicles and τ_{Zn} is the lifetime of the **1b** vesicles. The k_{ET} value was $3.1 \times 10^9\ s^{-1}$. The efficiency of this energy transfer (Φ_{ET}) could be determined to be 0.81 from Equation (3).[15]

$$\Phi_{ET} = k_{ET}/[k_{ET} + (1/\tau_{Zn})] \quad (3)$$

This non-covalently constructed **1a/1b** architecture showed relatively larger k_{ET} and Φ_{ET} than the values of the free-base/Zn^{2+} porphyrin dimers linked by covalent or hydrogen bonding.[2–5, 13] From the molecular area for lipid-porphyrin (2.2 nm^2), one vesicle (100 nm ϕ) is considered to consist of 23000 porphyrin molecules.[8c] To the best of our knowledge, this is the largest molecular energy transfer assembly made of self-organized porphyrin in water. For the triplet-state process, the transient difference absorption recorded in outgassed aqueous solution of the **1a/1b** vesicles did not show any significant peaks after the laser flash photolysis.

Electron transfer process of the lipid-porphyrin vesicles: In the lipid-porphyrin vesicles, the J-aggregated TPP platforms settled under the hydrophobic barrier of 4 nm thickness, and were not sensitive to the addition of a water-soluble electron acceptor or electron donor from the bulk aqueous phase. In fact, the fluorescence intensity of the **1a** or **1b** vesicles was not quenched at all by addition of electron acceptors; *N,N'*-methyl-4,4'-bipyridinium dichrolides and *N,N'*-benzyl-4,4'-bipyridinium dichrolides in the concentration range 0 to 2 mM. Since none of the quencher molecules caused a spectroscopic shift of the porphyrin absorption bands, there is no π-overlap between the electron accepting molecules and donating porphyrins. Attempting to reduce the Fe^{3+}TPP planes in the **1c** vesicles by addition of ascorbic acid also failed. These results imply that water-soluble molecules cannot enter the membrane interior. It is, therefore, certain

that the membrane properties should be modified to realize electron communications through the lipid-porphyrin membranes. Over the past few decades, substantial efforts have also been directed towards embedding two different porphyrins geometrically in phospholipid liposomes,[6f, 16] but the location of each co-factor is not always very accurate because of the low guest-to-host ratio in the membranes.

The free-base porphyrin **1a** was coassembled with protoporphyrin IX (PPIX) bearing two alkylphosphocholine propionates (**2**) (molar ratio: **1a**/**2** = 10), to give similar round vesicles. Although porphyrin **2** itself produced very thin monomolecular fibers in water (Figure 8a),[6d] the TEM observation showed only spherical unilamellars (ca. 100 nm

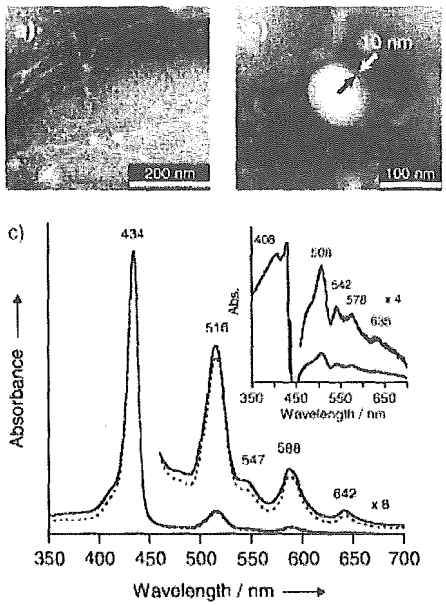

Figure 8. Transmission electron micrographs of the evaporated aqueous solutions of a) **2** and b) the **1a**/**2** ensemble (molar ratio: **1a**/**2** = 10); c) UV/Vis absorption spectra of **1a** vesicles (dotted line) and **1a**/**2** ensemble vesicles (solid line) in water at 25 °C. The inset shows a different spectrum for both solutions, in which the absorption maxima coincided with those of the DPPC vesicles incorporating **2** (molar ratio: DPPC/**2** = 40/1) in water.

ϕ) (Figure 8b). No fibrous aggregate was detectable and the membrane did not become thicker. Increasing the amount of **2** (molar ratio: **1a**/**2** < 5) led to deformation of the morphology into small micelles and fibers. The subtracted difference absorption spectrum of the **1a**/**2** hybrids minus the homogeneous **1a** vesicles showed λ_{max} at 408, 508, 542, 578, and 635 nm (Figure 8c inset). Unfortunately, the disturbance interfered with the Soret band region. It coincided with the absorption maxima of an aqueous solution of phospholipid liposomes (ex. 1,2-dipalmytoyl-3-*sn*-glycerophosphocholine (DPPC)) incorporating **2** (molar ratio: DPPC/**2** = 40, λ_{max}: 408, 509, 542, 579, and 634 nm). We concluded that **2** was homogeneously trapped into the highly oriented alkylene region of the **1a** vesicles without stacking. It may be presumed with certainty that the protoporphyrin macrocycle was anchored at the middle of the monolayer perpendicular to the membrane surface [see space-filling model in Figure 9b].

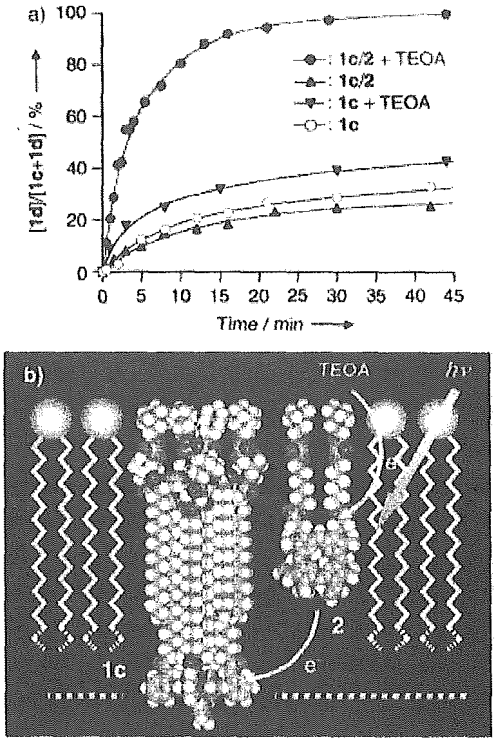

Figure 9. a) Photoreduction of Fe^{3+}TPP moieties of **1c**/**2**/DIm vesicles in aqueous phosphate buffer (pH 7.3) at 25 °C. b) The schematic representation of the **1c**/**2**/DIm monolayer membrane interior using the space-filling model for the each compound (DIm is replaced by 1-methylimidazole for clarification).

In the vesicles of the Fe^{3+} complex **1c** including free-base **2** (molar ratio: **1c**/**2** = 10), the fluorescence of the protoporphyrin chromophore was completely quenched. This decrease in the emission would be ascribed to the intermolecular electron transfer from the excited singlet state of **2** to **1c** within the vesicles. The Fe^{3+} porphyrins are *d*-typed hyperporphyrins with an extremely short lifetime of the excited state and no fluorescence. This quenching cannot be interpreted in terms of a static mechanism and is assumed to be due to oxidative quenching. An attempt to observe the time-resolved difference spectrum of the **2** cation radical was unsuccessful, because the absorption intensity of the protoporphyrin **2** was rather low, and the reaction rate was beyond the resolution of our apparatus. The excited triplet state of **2** may also be populated by means of intersystem crossing from the singlet state, which occurs in competition with the electron transfer, but the triplet–triplet absorption of **2** was not seen in the 500–900 nm region.

The coexistence of a small excess of 1-dodecylimidazole (DIm) as an axial base for the Fe^{3+} complex **1c** did not cause morphological changes in the vesicular configuration. The UV/Vis spectrum of the **1c**/**2**/DIm (molar ratio: 1/0.1/3) showed maxima at 544 and 575 nm, indicating that the dominant species of **1c** is a six-coordinate ferric complex with the axially bound bis-imidazole of DIm.[17] Under an argon atmosphere, the 390 nm (Soret band of **2**) photoirradiation of the **1c**/**2**/DIm vesicles with triethanolamine (TEOA) in the outer aqueous phase led to efficient and

irreversible reduction of the ferric ion of **1c**; the visible absorption spectrum changed to the typical six-*N*-coordinated low-spin Fe^{2+} complex (λ_{max}: 436, 538, and 568 nm).[8c, 18] The isosbestic points (534 and 562 nm) throughout the measurement revealed that no side reaction occurred. The following results indicate that the photoreduction of **1c** takes place through the intermolecular electron transfer initiated by excitation of **2**; 1) in the absence of TEOA or **2**, the reduction proceeded by less than 40% (Figure 9a), 2) irradiation of the Soret band of **1c** also reduced the ferric center, but by less than 30%. Photoirradiation of the Soret band of **2** causes only the efficient reduction of **1c**, and TEOA acts as a sacrificial reagent to reduce the cation radical of **2**. The protoporphyrin anchors successfully serve as an electron transfer mediator, and the space-filling model of the **1c/2**/DIm hybrid demonstrated well our supposed structure (Figure 9b). The overall process of this reaction is expressed by Equation (4), where LP is lipid-porphyrin and PP is the protoporphyrin moiety of **2**.

$$Fe^{3+}LP(DIm)_2 + PP \overset{h\nu}{\rightleftharpoons} Fe^{3+}LP(DIm)_2 + PP^* \rightleftarrows Fe^{2+}LP(DIm)_2 + PP^{+\cdot} \overset{e^-}{\rightleftharpoons} Fe^{2+}LP(DIm)_2 + PP \quad (4)$$

After reduction of **1c**, the membrane-trapped protoporphyrin becomes more hydrophilic and may be close enough to the bulk aqueous phase to accept an electron.

Upon exposure of the aqueous solution of the photoreduced **1d/2**/DIm vesicles to O_2, the UV/Vis absorption spectrum immediately changed to that of the corresponding O_2-adduct complex (λ_{max}: 435, 543 nm). This dioxygenation was observed to be reversibly dependent on the O_2-partial pressure the same as in our previous reported **1d**/DIm vesicles.[8c]

Conclusions

The perfectly round bilayer vesicles made of self-organized lipid-porphyrin **1a/1b** ensembles are the first molecular energy transfer assemblies with a diameter of over 100 nm in water. Singlet energy transfer occurs with a rate constant of $3.1 \times 10^9\ s^{-1}$ and with 81% efficiency. The non-covalently aligned J-aggregate porphyrins described herein have been shown to represent an effective approach to constructing a new class of light-harvesting antennae models in aqueous media. Indeed, effective optical cross-section per **1b** molecule in the vesicles at 558 nm is 0.73 Å^2, which is identical to that observed in benzene/MeOH homogeneous solution.[19] The 23000 porphyrin active sites are densely packed in the vesicles and isolated from the bulk aqueous solution; therefore electron communications to the outside of the membrane have some difficulties. However, anchoring of the protoporphyrin electron-mediator to the monolayer immediately permits funneling an electron by light irradiation, and it gave a hemoglobin-like property—reversible O_2-binding activity—to the vesicles. New investigations of a photoinduced charge separation process with an external electron acceptor and light-controllable heme catalytic reactions in these supramolecular lipid-porphyrin architectures are now being undertaken.

Experimental Section

Materials and apparatus: The synthetic methods for lipid-porphyrins (**1a**, **1c**, **2**) are described elsewhere.[8c, 6d] The Zn^{2+} complex **1b** was synthesized by the insertion of zinc into the free-base lipid-porphyrin **1a** using $Zn(OAc)_2$ in MeOH solution (yield: 85%). Triethanolamine, *N,N'*-methyl-4,4'-bipyridinium dichrolides, and *N,N'*-benzyl-4,4'-bipyridinium dichrolides of high-purity grade were used without further purification. UV/Vis absorption spectra were recorded on a JASCO V-570 spectrophotometer, and steady state fluorescence spectra were obtained from a HITACHI F-4500 spectrofluorometer. All these measurements were normally carried out at 25°C.

Preparation of aqueous lipid-porphyrin solutions:

*a) Lipid-porphyrin (**1a**, **1b**, **1a/1b**) solutions*: A benzene/methanol stock solution of **1a** or **1b** (50—100 μL, 1.0 mM) was placed in a 5 mL round-bottom flask and slowly condensed using a rotary evaporator under reduced pressure, affording a thin film of the porphyrin at the bottom. The film was then dried in vacuo for 3 h; deionized water (5 mL) heated at 60°C was slowly injected. The mixture was homogenized by vortex mixing with several small glass beads (ca. 10 pieces) and shortly sonicated by a bath-type ultrasonicator. The obtained solution (10–20 μM) was incubated for 6 h at room temperature before use. The hybridized **1a/1b** solution was also prepared in the same manner.

*b) Lipid-porphyrins **1a/2** and **1c/2**/1-dodecylimidazole (DIm) hybrid solutions*: A benzene/methanol stock solution of **1a** (100 μL, 1.0 mM) and methanol solution of **2** (10 μL, 1.0 mM) were slowly condensed by using a rotary evaporator under reduced pressure as described above, giving a hybrid thin-film at the bottom of the flask. The film was dried *in vacuo* for 3 h and phosphate buffer (pH 7.3, 1 mM, 5 mL) heated at 60°C was added. Homogenization by a tip-type ultrasonicator (60 mW, 3 min) in a water bath provided a pale orange solution ([**1a**] = 20 μM), which was incubated for 12 h at room temperature. The hybrid lipid-porphyrin **1c/2**/DIm (molar ratio: 1/0.1/3, [**1c**] = 20 μM) was also prepared by the same procedures.

Transmission electron microscopy (TEM): The negatively stained specimens for TEM were prepared as in previously reported procedures.[7c, 8h] The Cu grid surfaces were treated for a short period (5 s) by glow discharge using a JEOL HDF-400 to form a hydrophilic plane just before use. The obtained grids with the evaporated sample were observed in a JEOL JEM-100CX electron microscope at an acceleration voltage of 100 kV.

Exciton calculation: The overall excitonic interaction in the Zn^{2+}TPP bilayer model of **1b** was calculated based on our previously reported methods.[8c]

Near-field scanning optical microspectroscopy (NSOM): A droplet of **1a/1b** vesicle solution (20 μM) was pipetted onto freshly-cleaved highly-oriented pyrolytic graphite (HOPG STM-1, Advanced Ceramics Co.). After 1 min, excess fluid was carefully blotted off with filtration paper and the surface air-dried for another 30 min. NSOM measurements were carried out using a JASCO NFS-230 Scanning Near-Field Optical Microspectrometer in the illumination collection mode under ambient laboratory conditions. The samples were excited by a He-Cd laser (442 nm) with 0.1 mW intensity for 0.5 s, and the diameter of the light probe was 400 nm. Imaging was performed by displaying the fluorescence signal and the height signal simultaneously for 4 × 4 μm (21 × 21 points).

Excited-state lifetimes: Singlet lifetimes of the lipid-porphyrin vesicles were measured by using a HORIBA NAES-500 nanosecond fluorometer with an N_2 lamp (excitation side multicavity filter: ASAHI SPECTRA MZ0560, $\lambda = 560 \pm 2$ nm; emission side multicavity filter: MZ0610, $\lambda = 610 \pm 2$ nm). The samples were held in a cuvette (optical path length, 10 mm). The concentration of the lipid-porphyrin was 9.5 μM, and experiments were carried out at 25°C. Triplet lifetime measurements on a nanosecond time scale were performed by using a Unisoku TSP-600 time-resolved spectrophotometer system with a Continuum Surelite I-10 Q-switched Nd-YAG laser, which generated a second-harmonic (532 nm) pulse of 6 ns duration with an energy of 200 mJ per pulse (10 Hz).

Steady-state electron-transfer from excited 2 to 1c: Continuous light irradiations were performed with an ORIEL 450 W xenon arc-lamp model 66021 under an argon atmosphere (25°C). The **1c** solution was deaerated by argon bubbling before photoirradiation. The light was filtered with cutoff filter (HOYA UV-32) and a multicavity filter (ASAHI SPECTRA

MY0390, $\lambda = 390 \pm 2$ nm) to isolate the desired wavelength region. The filtered light was irradiated into a solution of the **1c**/DIm (molar ratio: 1/3) vesicles or **1c**/**2**/DIm vesicles (molar ratio: **1c**/**2**/DIm = 1/0.1/3) with (or without) triethanolamine (64 mM) contained in a 10 mm cuvette at a distance of 140 mm from the center of the light source. The UV/Vis absorption spectra of the solution were measured at regular intervals. The photoreduction of **1c** to the ferrous complex **1d** was monitored by the time dependence of the absorption intensity at 538 nm, which is based on the bisimidazole coordinated Fe^{2+} complex. In order to obtain a spectrum of the completely reduced ferrous **1d**/**2**/DIm vesicles, an aqueous sodium dithionate solution (25 mM, 40 μL) was added to the **1c**/**2**/DIm vesicle solution at 60 °C.

Acknowledgements

We thank the JASCO Corporation for the skilful observations of NSOM. This work was partially supported by a Grant-in-Aid for Scientific Research (No. 13650938) from the JSPS, and Health Science Research Grants (Research on Pharmaceutical and Medical Safety) from the MHLW.

[1] a) J. Deisenhofer, O. Epp, K. Miki, R. Huber, H. Michel, *Nature* **1985**, *318*, 618–624; b) G. Feher, J. P. Allen, M. Y. Okamura, D. C. Rees, *Nature* **1989**, *339*, 111–116; c) G. McDermott, S. M. Prince, A. A. Freer, A. M. Hawthornthwaite-Lawless, M. Z. Papiz, R. J. Cogdell, N. W. Isaacs, *Nature* **1995**, *374*, 517–521; d) S. M. Prince, M. Z. Papiz, A. A. Freer, G. McDemott, A. M. Hawthornthwaite-Lawless, R. J. Codgell, N. W. Isaacs, *J. Mol. Biol.* **1997**, *268*, 412–423; e) J. M. Olson, *Photochem. Photobiol.* **1998**, *67*, 61–75.

[2] a) M. R. Wasielewski, *Chem. Rev.* **1992**, *92*, 435–461; b) J. K. M. Sanders in *The Porphyrin Handbook, Vol. 3, Inorganic, Organometallic and Coordination Chemistry* (Eds.: K. M. Kadish, K. M. Smith, R. Guilard), Academic Press, New York, **1999**, Chapter 22.

[3] Examples of covalently bound multiporphyrinic assemblies made of more than three porphyrin units: a) S. Anderson, H. L. Anderson, A. Bashall, M. McPartlin, J. K. M. Sanders, *Angew. Chem.* **1995**, *107*, 1196–1200; *Angew. Chem. Int. Ed. Engl.* **1995**, *34*, 1096–1099; b) C. C. Mak, N. Bampos, J. K. M. Sanders, *Angew. Chem.* **1998**, *110*, 3169–3172; *Angew. Chem. Int. Ed.* **1998**, *37*, 3020–3023; c) H. A. M. Biemans, A. E. Rowan, A. Verhoeven, P. Vanoppen, L. Latterini, J. Foekema, A. P. H. J. Schenning, E. W. Meijer, F. C. de Schryver, R. J. M. Nolte, *J. Am. Chem. Soc.* **1998**, *120*, 11054–11060; d) M. G. H. Vicente, M. T. Cancilla, C. B. Lebrilla, K. M. Smith, *Chem. Commun.* **1998**, 2355–2356; e) A. Nakano, A. Osuka, I. Yamazaki, T. Yamazaki, Y. Nishimura, *Angew. Chem.* **1998**, *110*, 3172–3176; *Angew. Chem. Int. Ed.* **1998**, *37*, 3023–3027; f) N. Aratani, A. Osuka, Y.-H. Kim, D.-H. Jeong, D. Kim, *Angew. Chem.* **2000**, *112*, 1517–1521; *Angew. Chem. Int. Ed.* **2000**, *39*, 1458–1462; g) J. Li, A. Ambroise, S.-I. Yang, J. R. Diers, J. Seth, C. R. Wack, D. F. Bocian, D. Holten, J. S. Lindsey, *J. Am. Chem. Soc.* **1999**, *121*, 8927–8940; h) M.-S. Choi, T. Aida, T. Yamazaki, I. Yamazaki, *Angew. Chem.* **2001**, *113*, 3294–3298; *Angew. Chem. Int. Ed.* **2001**, *40*, 3194–3198; i) S. Rucareanu, O. Mongin, A. Schuwey, N. Hoyler, A. Gossauer, *J. Org. Chem.* **2001**, *66*, 4973–4988.

[4] J. L. Sessler, B. Wang, S. L. Spring, C. T. Brown in *Comprehensive Supramolecular Chemistry, Supramolecular Reactivity and Transport: Bioorganic Systems, Vol. 4* (Eds.: J.-M. Lehn, J. L. Atwood, J. E. D. Davies, D. D. MacNicol, F. Vögtle, Pergamon), Oxford, **1996**, pp. 311–336.

[5] Examples of noncovalently bound multiporphyrinic assemblies made of more than three porphyrin units: a) A. M. Brun, S. J. Atherton, A. Harriman, V. Heitz, J.-P. Sauvage, *J. Am. Chem. Soc.* **1992**, *114*, 4632–4639; b) M. Linke, J.-C. Chambron, V. Heitz, J.-P. Sauvage, S. Encinas, F. Barigelletti, L. Flamigni, *J. Am. Chem. Soc.* **2000**, *122*, 11834–11844; c) J. L. Sessler, B. Wang, A. Harriman, *J. Am. Chem. Soc.* **1995**, *117*, 704–714; d) H. L. Anderson, *Inorg. Chem.* **1994**, *33*, 972–981; e) G. S. Wilson, H. L. Anderson, *Chem. Commun.* **1999**, 1539–1540; f) C. A. Hunter, R. K. Hyde, *Angew. Chem.* **1996**, *108*, 2064–2067; *Angew. Chem. Int. Ed. Engl.* **1996**, *35*, 1936–1939; g) R. A. Haycock, A. Yartsev, U. Michelson, V. Sundström, C. A. Hunter, *Angew. Chem.* **2000**, *112*, 3762–3765; *Angew. Chem. Int. Ed.* **2000**, *39*, 3616–3619; h) P. Ballester, R. M. Gomila, C. A. Hunter, A. S. H. King, L. J. Twyman, *Chem. Commun.* **2003**, 38–39; i) C. M. Drain, K. C. Russel, J.-M. Lehn, *Chem. Commun.* **1996**, 337–338; j) J. Fan, A. Whiteford, B. Olenyuki, M. D. Levin, P. J. Stang, E. B. Fleischer, *J. Am. Chem. Soc.* **1999**, *121*, 2741–2752; k) A. Prodi, M. T. Indelli, C. J. Kleverlaan, F. Scandola, E. Alessio, T. Gianferrara, L. G. Marzilli, *Chem. Eur. J.* **1999**, *5*, 2668–2679; l) N. Maruo, M. Uchiyama, T. Kato, T. Arai, H. Akisada, N. Nishino, *Chem. Commun.* **1999**, 2057–2058; m) K. Ogawa, Y. Kobuke, *Angew. Chem.* **2000**, *112*, 4236–4239; *Angew. Chem. Int. Ed.* **2000**, *39*, 4070—4073; n) C. C. Mak, N. Bampos, S. L. Darling, M. Montalti, L. Prodi, J. K. M. Sanders, *J. Org. Chem.* **2001**, *66*, 4476–4486; o) M. Sakamoto, A. Ueno, H. Mihara, *Chem. Eur. J.* **2001**, *7*, 2449–2458; p) S. Yagai, T. Miyatake, H. Tamiaki, *J. Org. Chem.* **2002**, *67*, 49–58.

[6] R. Guilard, N. Senglet, Y. H. Liu, D. Sazou, E. Findsen, D. Fanre, T. D. Courieres, K. M. Kadish, *Inorg. Chem.* **1991**, *30*, 1898–1905; b) J.-H. Fuhrhop, C. Demoulin, C. Böttcher, J. Köning, U. Siggel, *J. Am. Chem. Soc.* **1992**, *114*, 4159–4165; c) J.-H. Fuhrhop, U. Bindig, U. Siggel, *J. Am. Chem. Soc.* **1993**, *115*, 11036–11037; d) E. Tsuchida, T. Komatsu, N. Toyano, S. Kumamoto, H. Nishide, *J. Chem. Soc. Chem. Commun.* **1993**, 1731–1733; e) T. Komatsu, K. Arai, H. Nishide, E. Tsuchida, *Chem. Lett.* **1993**, 1949–1952; f) T. Komatsu, E. Tsuchida, C. Böttcher, D. Donner, C. Messerschmidt, U. Siggel, W. Stocker, J. P. Rabe, J.-H. Fuhrhop, *J. Am. Chem. Soc.* **1997**, *119*, 11660–11665; g) C. Schell, H. K. Hombrecher, *Chem. Eur. J.* **1999**, *5*, 587–598; h) K. Kano, K. Fukuda, H. Wakami, R. Nishiyabu, R. F. Pasternack, *J. Am. Chem. Soc.* **2000**, *122*, 7494–7502; i) N. Nagata, S. Kugimiya, Y. Kobuke, *Chem. Commun.* **2001**, 689–690.

[7] a) T. Komatsu, K. Nakao, H. Nishide, E. Tsuchida, *J. Chem. Soc., Chem. Commun.* **1993**, 728–730; b) E. Tsuchida, T. Komatsu, K. Arai, K. Yamada, H. Nishide, C. Böttcher, J.-H. Fuhrhop, *Chem. Commun.* **1995**, 1063–1064; c) T. Komatsu, K. Yamada, E. Tsuchida, U. Siggel, C. Böttcher, J.-H. Fuhrhop, *Langmuir* **1996**, *12*, 6242–6249; d) T. Komatsu, T. Yanagimoto, E. Tsuchida, U. Siggel, J.-H. Fuhrhop, *J. Phys. Chem. B* **1998**, *102*, 6759–6765; e) T. Komatsu, T. Yanagimoto, Y. Furubayashi, J. Wu, E. Tsuchida, *Langmuir* **1999**, *15*, 4427–4433.

[8] a) E. Tsuchida, T. Komatsu, K. Arai, H. Nishide, *J. Chem. Soc., Chem. Commun.* **1993**, 730–732; b) E. Tsuchida, T. Komatsu, K. Arai, K. Yamada, H. Nishide, C. Böttcher, J.-H. Fuhrhop, *Langmuir* **1995**, *11*, 1877–1884; c) T. Komatsu, M. Moritake, A. Nakagawa, E. Tsuchida, *Chem. Eur. J.* **2002**, *8*, 5469–5480.

[9] a) E. G. McRae, M. Kasha, *J. Chem. Phys.* **1958**, *28*, 721–722; b) M. Kasha, *Radiation Res.* **1963**, *20*, 51–71.

[10] a) M. P. Byrn, C. J. Curtis, I. Goldberg, Y. Hsiou, S. I. Khan, P. A. Sawin, S. K. Tendick, C. E. Strouse, *J. Am. Chem. Soc.* **1991**, *113*, 6549–6557; b) M. P. Byrn, C. J. Curtis, Y. Hsiou, S. I. Khan, P. A. Sawin, S. K. Tendick, A. Terzis, C. E. Strouse, *J. Am. Chem. Soc.* **1993**, *115*, 9480–9497.

[11] The transition dipole moment was calculated by integrating plots of exciton coefficient divided by wavenumber, $\varepsilon(\nu)/\nu$, versus wavenumber ν and applying the equation $M^2 = 9.19 \times 10^{-3} \int[\varepsilon(\nu)/\nu]d\nu$, where M is the transition dipole moment in units of Debye.

[12] Based on the structural data reported by Strauce et al. (ref. [10]), the porphyrin core in the upper layer is supposed to locate on the +4.0, +2.7, and +4.1 Å shifts in the x, y, z directions from the center of each nearest pair in the layer below. The distances and angles from the porphyrin o to the neighbors P_{kl} in the upper layer were estimated. We then calculated all the interactions of these porphyrin pairs (total: 46 combinations), but stopped summation at a distance of some 5 nm.

[13] a) F. P. Schwarz, M. Gouterman, Z. Muljiani, D. H. Dolphin, *Bioinorg. Chem.* **1972**, *2*, 1–32; b) R. L. Brookfield, H. Ellul, A. Harriman, G. Porter, *J. Chem. Soc. Faraday Trans. 2* **1986**, *82*, 219–233; c) A. Osuka, K. Maruyama, I. Yamazaki, N. Tamai, *Chem. Phys. Lett.* **1990**, *165*, 392–396.

[14] D. M. Adams, J. Kerimo, C.-Y. Liu, A. J. Bard, P. F. Barbara, *J. Phys. Chem. B* **2000**, *104*, 6728–6736.

[15] Apparent energy transfer efficiency estimated from the steady state fluorescence intensity at 610 nm (Figure 5) was 0.61 (ref. [13b]).

[16] a) J. Lahiri, G. D. Fate, S. B. Ungashe, J. T. Groves, *J. Am. Chem. Soc.* **1996**, *118*, 2347–2358; b) C. R. Drain, *Proc. Natl. Acad. Sci. USA*, **2002**, 99, 5178–5182.

[17] a) F. A. Walker, M.-W. Lo, M. T. Ree, *J. Am. Chem. Soc.* **1976**, *98*, 5552–5560; b) R. Quinn, M. Nappa, J. S. Valentine, *J. Am. Chem. Soc.* **1982**, *104*, 2588–2595.

[18] a) J. P. Collman, R. R. Gagne, C. A. Reed, T. R. Halbert, G. Lang, W. T. Robinson, *J. Am. Chem. Soc.* **1975**, *97*, 1427–1439; b) J. R. Budge, P. E. Ellis, Jr., R. D. Jones, J. E. Linard, F. Basolo, J. E. Baldwin, R. L. Dyer, *J. Am. Chem. Soc.* **1979**, *101*, 4760–4762; c) M. Momenteau, B. Loock, E. Bisagni, M. Rougee, *Can. J. Chem.* **1979**, *57*, 1804–1813.

[19] a) D. Mauzerall, N. L. Greenbaum, *Biochim. Biophys. Acta* **1989**, *974*, 119–140; b) N. L. Greenbaum, D. Mauzerall, *Biochim. Biophys. Acta* **1991**, *1057*, 195–207.

Received: April 3, 2003 [F5013]

BMC Structural Biology

BioMed Central

Research article

Open Access

Crystal structural analysis of human serum albumin complexed with hemin and fatty acid

Patricia A Zunszain[1], Jamie Ghuman[1], Teruyuki Komatsu[2], Eishun Tsuchida[2] and Stephen Curry*[1]

Address: [1]Department of Biological Sciences, Imperial College London, Room 746 Huxley Building, South Kensington Campus, London SW7 2AZ, United Kingdom and [2]Advanced Research Institute for Science and Engineering, Waseda University, Tokyo 169-8555, Japan

Email: Patricia A Zunszain - p.zunszain@imperial.ac.uk; Jamie Ghuman - j.ghuman@imperial.ac.uk; Teruyuki Komatsu - teruyuki@waseda.jp; Eishun Tsuchida - eishun@mn.waseda.ac.jp; Stephen Curry* - s.curry@imperial.ac.uk

* Corresponding author

Published: 07 July 2003

BMC Structural Biology 2003, **3**:6

Received: 06 May 2003
Accepted: 07 July 2003

This article is available from: http://www.biomedcentral.com/1472-6807/3/6

Abstract

Background: Human serum albumin (HSA) is an abundant plasma protein that binds a wide variety of hydrophobic ligands including fatty acids, bilirubin, thyroxine and hemin. Although HSA-heme complexes do not bind oxygen reversibly, it may be possible to develop modified HSA proteins or heme groups that will confer this ability on the complex.

Results: We present here the crystal structure of a ternary HSA-hemin-myristate complex, formed at a 1:1:4 molar ratio, that contains a single hemin group bound to subdomain IB and myristate bound at six sites. The complex displays a conformation that is intermediate between defatted HSA and HSA-fatty acid complexes; this is likely to be due to low myristate occupancy in the fatty acid binding sites that drive the conformational change. The hemin group is bound within a narrow D-shaped hydrophobic cavity which usually accommodates fatty acid; the hemin propionate groups are coordinated by a triad of basic residues at the pocket entrance. The iron atom in the centre of the hemin is coordinated by Tyr161.

Conclusion: The structure of the HSA-hemin-myristate complex (PDB ID 1o9x) reveals the key polar and hydrophobic interactions that determine the hemin-binding specificity of HSA. The details of the hemin-binding environment of HSA provide a structural foundation for efforts to modify the protein and/or the heme molecule in order to engineer complexes that have favourable oxygen-binding properties.

Background

In the human body heme may be released into the circulation during enucleation of erythrocytes or through hemolytic injury. Free heme is immediately oxidized to the ferric state, hemin, which is potentially toxic since it may intercalate in lipid membranes and catalyze the formation of hydroxyl radicals and the oxidation of low density lipoproteins [1]. This toxicity is largely averted though the scavenging action of hemopexin, a protein that circulates in plasma (~17 μM), binds hemin with extremely high affinity (K_D < 1 pM) and transports it to various tissues – primarily liver cells – for intracellular catabolism [2].

Human serum albumin (HSA), the most abundant plasma protein (~640 μM) also has a high affinity for

hemin. The dissociation constant for the interaction was determined to be ~10 nM in a 3:5 (v/v) mix of dimethyl sulfoxide and water [3] but the interaction is likely to be even tighter in a more aqueous medium. HSA may provide a reserve binding capacity for situations when hemopexin becomes saturated. The protein is principally characterized by its remarkable ability to bind a broad range of hydrophobic small molecule ligands including fatty acids, bilirubin, thyroxine, bile acids and steroids; it serves as a solubilizer and transporter for these compounds and, in some cases, provides important buffering of the free concentration [4]. HSA also binds a wide variety of drugs in two primary sites [5,6] which overlap with the binding locations of endogenous ligands. The protein is a helical monomer of 66 kD containing three homologous domains (I-III) each of which is composed of A and B subdomains [5]. Despite the internal structural symmetry, the three domains have different capacities for binding fatty acids [7–10], thyroxine [11] and drugs [5,8,12,13]. Binding studies indicate a single site for hemin in subdomain IB [14] which corresponds to a binding site for fatty acids [8–10].

The ability of HSA to bind hemin has stimulated efforts to develop HSA-heme complexes that mimic the reversible oxygen-binding properties of heme proteins such as myoglobin and hemoglobin. One difficulty with this approach is that even if HSA-bound hemin is reduced to heme, stable and reversible oxygen binding by the complex cannot be observed (reviewed in [15,16]), because the heme binding site does not provide a molecular environment sufficiently similar to that found in myoglobin or hemoglobin. However, recent work has shown that artificial heme derivatives associate with HSA and provide significant oxygen-binding capacity [15,17–21]. Although such compounds have extensive modifications to the porphyrin ring and are not expected to bind to the protein in the same fashion as heme, they represent a promising line of inquiry for the development of artificial blood substitutes.

In order to advance our understanding of the heme-binding properties of HSA and the development of viable blood substitutes based on HSA-heme complexes, we have solved the crystal structure of a HSA-hemin-myristate complex. The structure reveals a previously undetected conformational state of the protein and provides a detailed view of the heme binding site. Our results are compared with a recently reported structure for methemalbumin [22].

Results and Discussion

Overall structure of the complex

The complex of HSA with hemin and myristate was prepared using a HSA:hemin:myristate mole ratio of 1:1:4 (Materials and Methods). The crystal structure was solved by molecular replacement and refined to a resolution of 3.2 Å. The refined model has an R_{free} value of 28.8% and good stereochemistry (Table 1). It contains a single molecule of hemin bound to the hydrophobic cavity in subdomain IB and myristates bound at six sites on the protein (Figure 1a). These correspond to fatty acid sites 2–7 which were identified in our previous work [8,9]. Fatty acid site 1 is occupied by hemin under our experimental conditions and prevents fatty acid binding by steric exclusion.

The electron density clearly indicates the binding configuration of the porphyrin ring and the two propionate groups of the bound hemin (Figure 1b), though it is possible that the molecule binds in two overlapping orientations that are related by a two-fold rotation (180°) about its centre. In either of the two orientations the propionate groups appear to be able to make the same interactions with the protein (to residues R114, H146 and K190) but the asymmetric location of the vinyl groups projecting from the hydrophobic end of the hemin molecule would occupy different positions. From the structure it appears that both configurations of the vinyl group could be accommodated within the binding pocket but may result in small adjustments of sidechains lining the pocket and of the exact position of the porphryin ring and its iron centre. Even at higher resolution, this ambiguity is not resolved [22] and it may therefore reflect a genuine degeneracy in hemin binding.

The density for the fatty acids is generally rather weak, indicating partial occupancy as would be expected given the 4:1 mole ratio of fatty acid to HSA used to prepare the complex. Although there is usually clear density to indicate the position of the fatty acid carboxylate moiety in each binding pocket, the density for the methyl end of the methylene tail is weak or absent. As a result, only the visible portion of the fatty acid tails has been included in the refined model.

Conformational changes

A surprising finding is that the HSA-hemin-myristate complex adopts a conformation that is intermediate between the structure of unliganded HSA [5,12,23] and that observed previously for HSA-fatty acid complexes [8–10]. The structural changes associated with fatty acid binding in previous work can be regarded essentially as rigid-body rotations of domains I and III relative to II that pivot around the mid-point of the long inter-domain helices (Figures 2a and 2b) and are driven primarily by binding of fatty acids to the I-II and II-III interfaces, though contacts between domains I and III may also be involved [8,24]. This conformational change appears to be independent of the length or degree of unsaturation of the fatty acid methylene tail [9,10] though it must be borne in

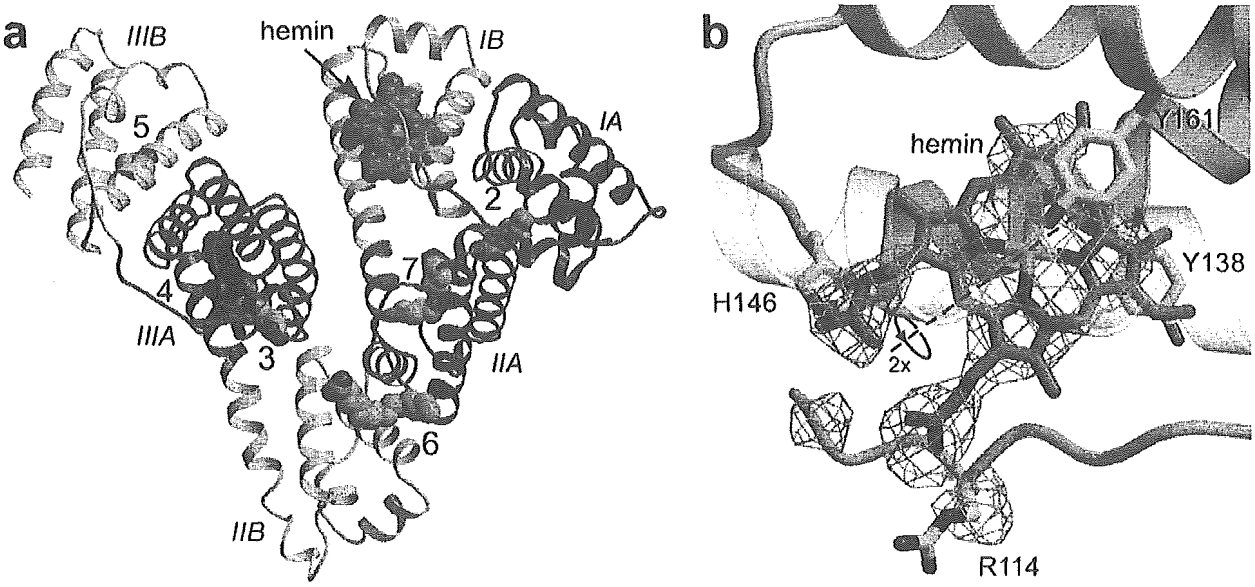

Figure 1

Crystal structure of the HSA-myristate-hemin complex (a) The protein secondary structure is shown schematically with the sub-domains colour-coded as follows: IA, red; IB – light red; IIA, green; IIB – light-green; IIIA, blue; IIIB – light blue; this colour scheme is maintained throughout. Ligands are shown in a space-filling representation, coloured by atom type: carbon – grey; nitrogen – blue; oxygen – red; iron – orange. Fatty acid binding sites are labelled 2–7. Except where stated otherwise, molecular graphics were prepared using Bobscript [32] and Raster3D [33]. **(b)** An F_{obs}-F_{calc} simulated annealing omit map [30] contoured at 2.5σ for hemin bound to subdomain IB. Selected amino acid sidechains are shown coloured by atom type. The dashed line indicates the two-fold symmetry axis that may relate alternative binding configurations of the porphyrin ring. The helix which overlies the bound hemin (residues 174–196) has been rendered semi-transparent.

mind that in these studies HSA-fatty acid complexes were prepared for crystallisation using a large molar excess of fatty acid to protein (>10:1) [9,10]. For the present investigation a 1:1 HSA-hemin complex was incubated with 4 moles of myristate per mole of HSA and then concentrated in a single step prior to crystallisation (see Materials and Methods). The crystals obtained belong to space-group $P2_12_12$, which has not previously been observed for HSA and was an early indication of the potential novelty of the conformational state. As observed for HSA-fatty acid complexes, the conformation of the HSA-hemin-myristate complex comprises changes from the unliganded state involving rigid-body rotations of domains I and III with respect to domain II; however in this case the particular rotation of domain I relative to domain II is only about 85% complete when compared to that observed in other HSA-fatty acid complex structures (Figures 2a and 2b). The difference in the orientation of domain III relative to domain II in the HSA-hemin-myristate and other HSA-fatty acid complexes [8–10,24] is rather small and may be due to differences in crystal packing.

It is conceivable that the difference in the orientation of domain I relative to domain II in the HSA-hemin-myristate and other HSA-fatty acid complexes is also due to changes in the crystal-packing environment between the two crystal forms ($P2_12_12$ and C2). However, consideration of the structure suggests that it is more likely to be due to differences in the level of bound fatty acid (Figures 2c and 2d). The crystal structure of the HSA-myristate complex – prepared using a high myristate:HSA mole ratio – showed evidence for two fatty acid molecules bound in a tail-to-tail configuration in the contiguous fatty acid sites 2 and 2' which straddle the interface between domains I and II. Occupancy of site 2 is believed to be primarily responsible for driving the conformational change between these two domains (Figure 2d). In the HSA-hemin-myristate complex, there is no evidence for fatty acid binding to site 2' and indeed the density for the fatty acid bound to site 2 is relatively weak, probably as a

result of the reduced occupancy (Figure 2c). Thus it may be that binding to site 2' is required to drive the more extensive conformational change between domains I and II. Although fatty acids longer than C14 are not observed to occupy site 2', they nevertheless appear to drive the "full" conformational change; this is most likely because the methylene tail of a long-chain fatty acid bound to site 2 begins to occupy site 2' [9,10] and may therefore play the same structural role as the binding of a second molecule of a shorter-chain fatty acid to site 2'. An independent crystallographic study on hemin binding to HSA in the presence of myristate reportedly obtained a conformation very similar to that found for HSA-myristate at very high myristate:HSA mole ratios [8], but the amount of myristate used was not given and the coordinates are not yet available to allow a direct comparison with our present structure [22]. Whatever the precise mechanism underlying the fatty-acid induced conformational changes, there is no evidence to suggest a connection between binding of hemin and the new conformational stage identified in the present work. Moreover, it is likely that the hemin-binding site itself is not affected by fatty acid induced conformational changes.

Table 1: Data collection and refinement statistics

DATA COLLECTION	
a (Å)	80.08
b (Å)	202.70
c (Å)	39.37
Resolution range (Å)	27.2–3.2
Independent reflections	10,825
Multiplicity[1]	2.7(2.6)
Completeness (%)	96.2(92.4)
I/σ	8.1(2.1)
R_{merge}(%)[2]	5.7(34.5)
MODEL REFINEMENT	
Nonhydrogen atoms	4479
R_{model} (%)[3]	28.8
R_{free} (%)[4]	23.1
r.m.s deviation from ideal bond lengths (Å)	0.007
r.m.s deviation from ideal angles (°)	1.4
Average B-factor (Å²)	75.3
PBD ID	1o9x

[1]Values for the outermost resolution shell are given in parentheses. [2] $R_{merge} = 100 \times \sum_h \sum_j |I_{hj} - I_h| / \sum_h \sum_j I_{hj}$ where I_h is the weighted mean intensity of the symmetry related reflections I_{hj} [3] $R_{model} = 100 \times \sum_{hkl} |F_{obs} - F_{calc}| / \sum_{hkl} F_{obs}$ where I_h where F_{obs} and F_{calc} are the observed and calculated structure factors respectively. [4] R_{free} is the R_{model} calculated using a randomly selected 5% sample of reflection data omitted from the refinement.

Details of the hemin binding site

Hemin binds to a hydrophobic, D-shaped cavity in subdomain IB. The hydrophobic porphyrin ring is essentially buried in the core of the subdomain with the propionate groups located at the wide entrance to the pocket where they can interact with solvent and several basic amino acid sidechains (see below). In the absence of ligand this cavity is partially occluded by two tyrosine residues (138 and 161) which stack on top of one another [24]. Upon hemin binding both sidechains undergo χ_1 rotations of around 90° thereby opening up the binding pocket and helping to clamp the ligand in place. Very similar rotations of these sidechains were observed with fatty acid binding [9]; indeed there is complete overlap between the positions of fatty acid and hemin when bound in this site. Other sidechains, including Leu139, His146, Ile142 and Leu154, exhibit modest adjustments upon heme binding.

There is a slight expansion of subdomain IB upon binding of hemin: the separation of helices 8 and 10 on either side of the ligand increases by about 1.4 Å. A similar sized expansion was also observed for fatty acid binding to this pocket [8]. The expansion may be constrained by the disulfide bridge between Cys124 and Cys169 that links helices 7 and 9 respectively (Figure 3a).

All of the structural components of subdomain IB, including the polypeptide linker connecting it to subdomain IA and helices 7–10, contribute to the hemin binding site. The hemin group binds with its plane oriented at about 30° to the directional axes of helices 8–10; this orientation is determined by the packing of the hemin group against the residues lining the interior wall of the pocket. With the exception of Tyr138 and Tyr161, these are entirely hydrophobic sidechains. The hydroxyl group of Tyr138 is relocated to the exterior of the domain where it interacts with solvent, but the hydroxyl group of Tyr161 makes a direct interaction with the central Fe^{3+} atom, providing a fifth point of coordination (Figure 3b). The entrance to the pocket, which is rather open, faces towards the interdomain cleft and contains three basic residues that coordinate the two propionate groups on hemin. Lys190 adopts a central position and makes salt-bridges to both propionate groups (2.7 and 3.0 Å); His146 provides a second electrostatic interaction with one heme carboxylate (3.0 Å) while the guanidinium group of Arg114 interacts with the other (2.8 Å). Arg117, which lies towards the top end of the pocket entrance and invariably interacts with fatty acids which bind at this site [9], is not involved in coordinating the propionate groups of the hemin. The electrostatic interactions to the propionate groups are clearly important for hemin binding; the number of residues involved in coordinating the propionate groups is fewer that the seven observed in hemopexin [25] but more than the one or two basic residues found to fill this

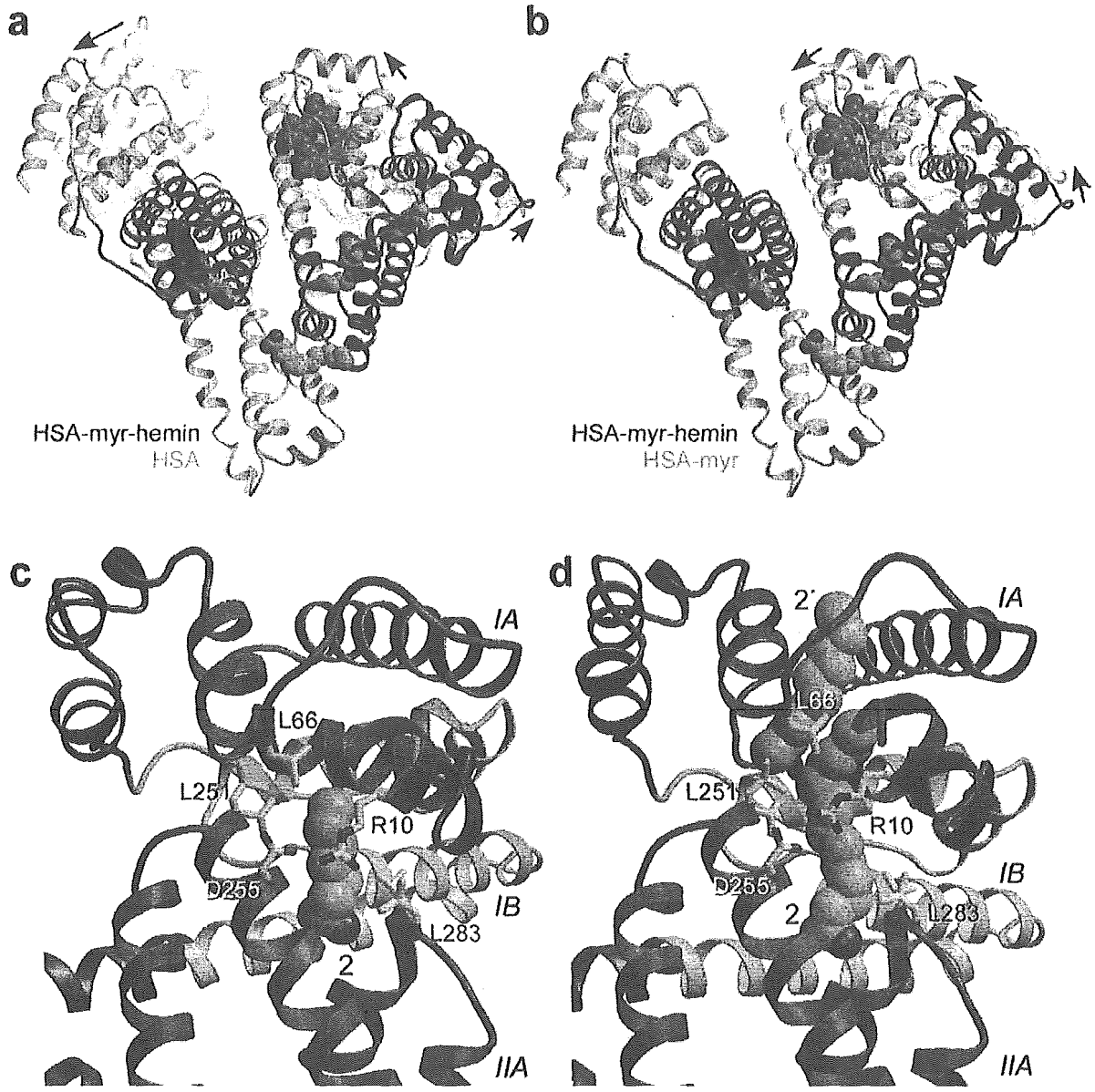

Figure 2

Conformational changes associated with variations in fatty acid content (a) Superposition of HSA-hemin-myristate (opaque) on defatted HSA (semi-transparent). **(b)** Superposition of HSA-hemin-myristate (opaque) on HSA-myristate (semi-transparent). HSA-hemin-myristate was prepared with a 4-fold molar excess of fatty acid whereas the HSA-myristate complex was prepared with a 12-fold molar excess [9] which saturates the binding sites. The colour scheme is the same as Figure 1. In each case the structures were superposed using the C_α atoms from domain II (residues 197–383). Arrows indicate the relative domain movements. **(c)** Close-up views of myristate binding site 2 which traverses the interface between domains I and II for HSA-hemin-myristate. Selected amino acid sidechains are shown coloured by atom type. The fatty acid is depicted in a space filling-representation. Only the first seven carbon atoms of the methylene tail for which there is clear electron density are shown; the remainder of the tail is disordered but presumable extends further upward. **(d)** A similar close-up view of the same site in the HSA-myristate structure [9]. In this case the site is occupied by two fatty acid molecules in a tail-to-tail configuration. The upper part of fatty acid site 2 is labelled 2'. The additional relative movement of the two domains at the higher fatty acid concentration is evident from the relative dispositions of R10 and D255, which interact across the top of the bound fatty acid.

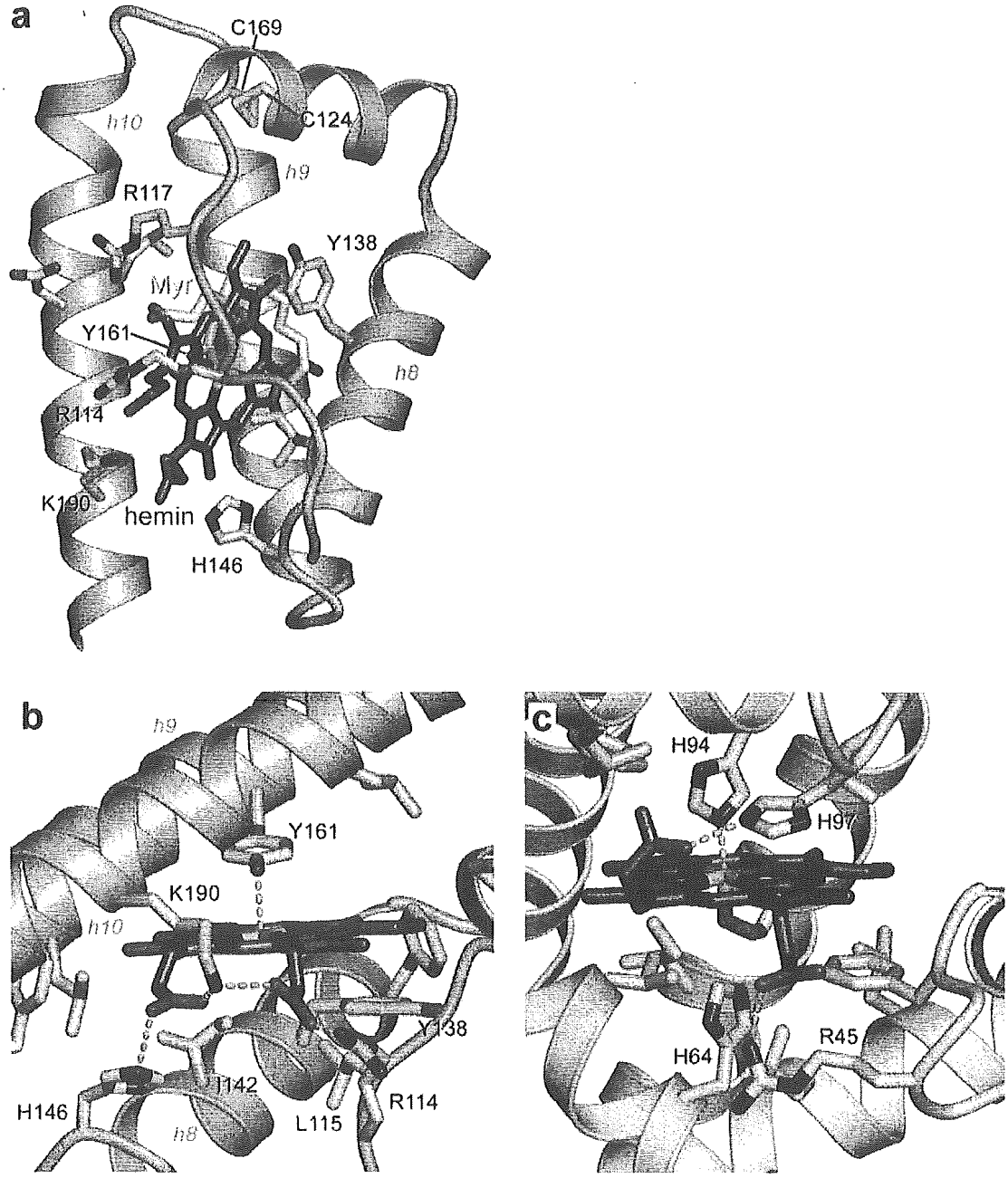

Figure 3

Detailed structure of the hemin-binding site in HSA and comparison with myoglobin (a) Side-view of subdomain IB of HSA indicating the comparative binding configurations of hemin (grey carbon atoms) and myristate (yellow carbon atoms). Helices 8–10 are labelled h8-h10. The structures of HSA-hemin-myristate and HSA-myristate [9] were superposed using the C_α atoms of subdomain IB (residues 107–196). The myristate lies along the upper hydrophobic surface of the D-shaped cavity that accommodates hemin. Note that R117, which serves to coordinate the carboxylate group of myristate, is not involved in this function for hemin. **(b)** Close-up view of the hemin-binding pocket in subdomain IB. The propionate groups of hemin are co-ordinated by R114, H146 and K190. **(c)** Close-up view of the heme-binding pocket of sperm-whale myoglobin (PDB ID: 4 mbn). Electrostatic interactions between protein side-chains and hemin are indicated by dashed cyan lines. This figure was prepared using Molscript [34] and Pymol [35].

role in myoglobin or hemoglobin (Figure 3c). At the opposite end of the pocket there is a small opening which is large enough to admit solvent molecules.

In terms of the general hydrophobicity of the pocket and the coordination of the propionate groups by basic residues, HSA appears to have similar features to the heme binding site on myoglobin or hemoglobin. However, although both proteins are helical there is little similarity in the architectures of their heme binding pockets. In particular, HSA lacks the pair of histidine residues that serve to enhance and regulate the relative oxygen- and carbon monoxide-binding properties of myoglobin and hemoglobin. Modification of the heme-binding pocket on HSA or of the heme-group itself is likely to be required to achieve a protein-heme complex capable of reversible oxygen binding. Although various heme derivatives have been produced that exhibit reversible oxygen binding in association with HSA [19–21,26], these contain sizeable additions to the porphyrin ring structure and are unlikely to bind to subdomain IB on HSA in the same configuration that has been observed for hemin. Nevertheless, the detailed architecture of the heme-binding pocket as revealed by this crystallographic study will facilitate the design of new heme derivatives that will be better accommodated in this site and may therefore bind with higher affinity. It will also enable the design of mutagenesis experiments to tailor the pocket to bind modified hemes.

Conclusions

The structure of the HSA-hemin-myristate complex reported here reveals a new conformational state of the protein, one that is intermediate between unliganded HSA and the saturated HSA-fatty acid complex. The observation of this conformation is likely due to the use of subsaturating amounts of fatty acid in preparing the crystals and provides new insights into the mechanism of conformational change.

The single hemin-binding pocket in subdomain IB of HSA consists of a deep hydrophobic slot that provides three basic residues at its entrance to coordinate the two propionate groups of the hemin. This provides a framework for future attempts to engineer the protein and heme derivative in order to generate high-affinity HSA-heme complexes which bind oxygen reversibly and may serve as effective artificial blood substitutes.

Methods

Preparation and crystallization of the HSA-hemin-myristate complex

Recombinant HSA (Recombin®), kindly provided by Delta Biotechnology (Nottingham, UK), was defatted and purified by gel filtration to be dimer-free in 50 mM potassium phosphate, 50 mM NaCl, pH 7.0 to a concentration of 110 mg/ml (1.67 mM) essentially as described previously [12]. Immediately prior to use hemin was dissolved at 10 mM in dimethylsulfoxide (DMSO) in a foil-wrapped microcentrifuge tube. The hemin and HSA solutions were mixed to give a hemin:HSA molar ratio of 1.1 to 1.0, and incubated with rotation in the dark at room temperature for at least 12 hours. The resulting complex was then concentrated using a 10 kDa molecular weight cut-off ultrafiltration device (Vivaspin, Millipore), and washed in repeated cycles of concentration and dilution with 50 mM potassium phosphate buffer, pH 7.0 to reduce the final concentration of DMSO < 0.1% (v/v). Myristic acid was freshly dispersed with the aid of mild heating in 20 mM potassium phosphate pH 7.0 to obtain a suspension with a concentration of 2.5 mM. The HSA-hemin complex was incubated with myristic acid, at a fatty acid:HSA molar ratio of 4:1, by rotation at room temperature for one hour. The complex was then concentrated – in a single step – in a Vivaspin ultrafiltration device and analysed on a polyacrylamide gel to estimate the protein concentration.

Crystals were grown by sitting-drop vapour diffusion at 4 °C using methods similar to those described previously [8,9,27]. Crystallization screens were set up at a protein concentration of >90 mg/ml using 20 to 40% PEG 3350 (Sigma-Aldrich) in 50 mM potassium phosphate buffer, pH 7.0 as the precipitant; the sitting drop initially contained 3.5 μl of the protein solution and 3.5 μl of the reservoir mixture. Three days after streak-seeding, crystals were observed at 24, 26, 28 and 30% PEG; the largest crystals were observed at 24 and 26 % PEG.

Data collection, processing, structure determination and refinement

X-ray diffraction data were collected at Daresbury SRS (station 9.6) and EMBL/DESY Hamburg (beamline X11) using crystals mounted in sealed glass capillaries maintained at room temperature. The data were indexed and measured with MOSFLM and scaled with SCALA [28]. The crystals belong to space-group $P2_12_12$. Efforts to solve the phase problem by molecular replacement with AMoRe [29] produced a promising solution for domain II of the protein (residues 197–383) taken from the HSA-myristate structure (PDB ID 1e7g) [9]; however, orientations for domains I and III were not found. Since the solution for domain II appeared to yield a sensible packing arrangement for HSA molecules in the unit cell, it was used as a starting point for rigid-body refinement using CNS [30]. The HSA-myristate model (1e7g) was initially refined as a single rigid body using data from 10–30 Å; thereafter, the protein was split into three domains (5–196, 197–383, 384–584) which were allowed to move independently and rigid body refinement was applied as the high resolution limit of the incorporated data was extended in 1 Å steps from 10 Å to 4 Å and finally to 3.2 Å. During this

process, the R_{free} (defined in table 1) dropped from 51.3% to 34.5%. An electron density map calculated at this stage showed clear electron density for the whole protein and the ligand molecules. Manual building in O [31] was interspersed with rounds of positional and group temperature factor refinement. Data collection and refinement statistics are summarized in Table 1.

Authors' contributions

PZ prepared and crystallized the complex and participated in data collection and processing. JG obtained the initial crystallisation conditions for HSA-myristate-hemin complexes and assisted with data collection. ET and TK participated in the design of the study and advised on hemin handling. SC participated in the design and coordination of the study, assisted in data collection and processing, refined the structure and drafted the manuscript. All authors read and approved the final manuscript.

Acknowledgements

We thank Delta Biotechnology (UK) for providing purified recombinant HSA (Recombumin®). We are indebted to the staff at Daresbury SRS (station 9.6) and EMBL/DESY Hamburg (X11) for assistance with data collection. JG is grateful for the award of an MRC studentship. This work was funded with grant support from the BBSRC (SC) and partially supported by the Health Science Research Grants (Research on Pharmaceutical and Medical Safety) for the MHLW.

References

1. Jeney V, Balla J, Yachie A, Varga Z, Vercellotti GM, Eaton JW and Balla G: **Pro-oxidant and cytotoxic effects of circulating heme** *Blood* 2002, **100:**879-887.
2. Tolosano E and Altruda F: **Hemopexin: structure, function, and regulation** *DNA Cell Biol* 2002, **21:**297-306.
3. Adams PA and Berman MC: **Kinetics and mechanism of the interaction between human serum albumin and monomeric haemin** *Biochem J* 1980, **191:**95-102.
4. Peters T: **All about albumin: biochemistry, genetics and medical applications** *San Diego, Academic Press*; 1995.
5. He XM and Carter DC: **Atomic structure and chemistry of human serum albumin** *Nature* 1992, **358:**209-215.
6. Sudlow G, Birkett DJ and Wade DN: **The characterization of two specific drug binding sites on human serum albumin** *Mol Pharmacol* 1975, **11:**824-832.
7. Hamilton JA, Era S, Bhamidipati SP and Reed RG: **Locations of the three primary binding sites for long-chain fatty acids on bovine serum albumin** *Proc Natl Acad Sci USA* 1991, **88:**2051-2054.
8. Curry S, Mandelkow H, Brick P and Franks N: **Crystal structure of human serum albumin complexed with fatty acid reveals an asymmetric distribution of binding sites** *Nature Structural Biology* 1998, **5:**827-835.
9. Bhattacharya AA, Grüne T and Curry S: **Crystallographic analysis reveals common modes of binding of medium and long-chain fatty acids to human serum albumin** *J Mol Biol* 2000, **303:**721-732.
10. Petitpas I, Grüne T, Bhattacharya AA and Curry S: **Crystal structures of human serum albumin complexed with monounsaturated and polyunsaturated fatty acids** *J Mol Biol* 2001, **314:**955-960.
11. Petitpas I, Petersen CE, Ha CE, Bhattacharya AA, Zunszain PA, Ghuman J, Bhagavan NV and Curry S: **Structural basis of albumin-thyroxine interactions and familial dysalbuminemic hyperthyroxinemia** *Proc Natl Acad Sci USA* 2003, **100:**6440-6445.
12. Bhattacharya AA, Curry S and Franks NP: **Binding of the general anesthetics propofol and halothane to human serum albumin: high-resolution crystal structures** *J Biol Chem* 2000, **275:**38731-38738.
13. Petitpas I, Bhattacharya AA, Twine S, East M and Curry S: **Crystal structure analysis of warfarin binding to human serum albumin: anatomy of drug site 1** *J Biol Chem* 2001, **276:**22804-22809.
14. Dockal M, Carter DC and Ruker F: **The three recombinant domains of human serum albumin. Structural characterization and ligand binding properties** *J Biol Chem* 1999, **274:**29303-29310.
15. Tsuchida E, Ando K, Maejima H, Kawai N, Komatsu T, Takeoka S and Nishide H: **Properties of and oxygen binding by albumin- tetraphenylporphyrinatoiron(II) derivative complexes** *Bioconjug Chem* 1997, **8:**534-538.
16. Marden MC, Hazard ES, Leclerc L and Gibson QH: **Flash photolysis of the serum albumin-heme-CO complex** *Biochemistry* 1989, **28:**4422-4426.
17. Komatsu T, Hamamatsu K, Takeoka S, Nishide H and Tsuchida E: **Human serum albumin-bound synthetic hemes as an oxygen carrier: determination of equilibrium constants for heme binding to host albumin** *Artif Cells Blood Substit Immobil Biotechnol* 1998, **26:**519-527.
18. Komatsu T, Matsukawa Y and Tsuchida E: **Kinetics of CO and O2 binding to human serum albumin-heme hybrid** *Bioconjug Chem* 2000, **11:**772-776.
19. Tsuchida E, Komatsu T, Hamamatsu K, Matsukawa Y, Tajima A, Yoshizu A, Izumi Y and Kobayashi K: **Exchange transfusion with albumin-heme as an artificial O2-infusion into anesthetized rats: physiological responses, O2-delivery, and reduction of the oxidized hemin sites by red blood cells** *Bioconjug Chem* 2000, **11:**46-50.
20. Tsuchida E, Komatsu T, Matsukawa Y, Nakagawa A, Sakai H, Kobayashi K and Suematsu M: **Human serum albumin incorporating synthetic heme: Red blood cell substitute without hypertension by nitric oxide scavenging** *J Biomed Mater Res* 2003, **64A:**257-261.
21. Tsuchida E, Komatsu T, Matsukawa Y, Hamamatsu K and Wu J: **Human serum albumin incorporating Tetrakis(o-pivalamido) phenylporphinatoiron(II) derivative as a totally synthetic O2-carrying hemoprotein** *Bioconjug Chem* 1999, **10:**797-802.
22. Wardell M, Wang Z, Ho JX, Robert J, Ruker F, Ruble J and Carter DC: **The atomic structure of human methemalbumin at 1.9 Å** *Biochem Biophys Res Commun* 2002, **291:**813-819.
23. Sugio S, Kashima A, Mochizuki S, Noda M and Kobayashi K: **Crystal structure of human serum albumin at 2.5 Å resolution** *Protein Eng* 1999, **12:**439-446.
24. Curry S, Brick P and Franks NP: **Fatty acid binding to human serum albumin: new insights from crystallographic studies** *Biochim Biophys Acta* 1999, **1441:**131-140.
25. Paoli M, Anderson BF, Baker HM, Morgan WT, Smith A and Baker EN: **Crystal structure of hemopexin reveals a novel high-affinity heme site formed between two beta-propeller domains** *Nat Struct Biol* 1999, **6:**926-931.
26. Komatsu T, Matsukawa Y and Tsuchida E: **Effect of heme structure on O2-binding properties of human serum albumin-heme hybrids: intramolecular histidine coordination provides a stable O2-adduct complex** *Bioconjug Chem* 2002, **13:**397-402.
27. Carter DC, Chang B, Ho JX, Keeling K and Krishnasami Z: **Preliminary crystallographic studies of four crystal forms of serum albumin** *Eur J Biochem* 1994, **226:**1049-1052.
28. Collaborative Computer Project No. 4.: **The CCP4 suite: programs for protein crystallography** *Acta Crystallogr.* 1994, **D50:**760-763.
29. Navaza J: **Implementation of molecular replacement in AMoRe** *Acta Crystallogr.* 2001, **D57:**1367-1372.
30. Brünger AT, Adams PD, Clore GM, DeLano WL, Gros P, Grosse-Kunstleve RW, Jiang JS, Kuszewski J, Nilges M, Pannu NS, Read RJ, Rice LM, Simonson T and Warren GL: **Crystallography & NMR system: A new software suite for macromolecular structure determination** *Acta Crystallogr.* 1998, **D54:**905-921.
31. Jones TA, Zou JY, Cowan SW and Kjeldgaard M: **Improved methods for building protein models in electron density maps and the location of errors in these maps** *Acta Crystallogr.* 1991, **A47:**110-119.
32. Esnouf R: **An extensively modified version of Molscript that includes greatly enhanced colouring capabilities** *J Mol Graphics* 1997, **15:**133-138.

33. Merrit EA and Bacon DJ: **Raster3D - photorealistic molecular graphics** *Methods in Enzymology* 1997, **277:**505-524.
34. Kraulis PJ: **MOLSCRIPT: a program to produce both detailed and schematic plots of protein structures** *J App Crystallogr* 1991, **24:**946-950.
35. Delano WL: **The PyMOL molecular graphics system** *San Carlos, CA, USA, DeLano Scientific*; 2002.

Coordination Structure of Active Site in Synthetic Hemoprotein (Albumin-Heme) with Dioxygen and Carbon Monoxide

Eishun Tsuchida, Akito Nakagawa, Teruyuki Komatsu*

Advanced Research Institute for Science and Engineering, Waseda University, Tokyo 169-8555, Japan

Summary: Recombinant human serum albumin (rHSA) incorporating the tetraphenylporphinatoiron(II) derivative with a covalently linked proximal base (FeP) [albumin-heme (rHSA-FeP)] is a synthetic hemoprotein, which can bind and release dioxygen (O_2) reversibly under physiological conditions. The coordination structure and spin-state of the active site in rHSA-FeP with O_2 and carbon monoxide (CO) were revealed by magnetic circular dichroism (MCD), resonance Raman (RR), and infrared (IR) spectroscopy. Under an N_2 atmosphere, the MCD spectrum of rHSA-FeP showed the formation of the five-coordinate ferrous high-spin complex of FeP. Upon exposure of this solution to O_2 or CO, the spectral pattern immediately changed to that of a six-coordinate ferrous low-spin species. The vibration stretching frequencies of the coordinated O_2 (ν_{O2}) and CO (ν_{CO}) were observed at 1158 cm^{-1} and 1964 cm^{-1}, respectively. The electronic structures of the O_2- and CO-adduct complexes of FeP in the hydrophobic pocket of albumin are both identical to those for FeP itself in toluene solution.

Keywords: albumin-heme; biomimetic; infrared spectroscopy; magnetic circular dishroism spectroscopy; O_2-adduct complex

Introduction

Human serum albumin (HSA) is the major plasma protein in our blood circulatory system, and it binds a great variety of metabolites and drugs.[1] The most well-known ligands for HSA are fatty acids, billilubin, and hemin. Hemin dissociated from the methemoglobin is immediately scavenged by HSA and safely transported to the liver for metabolism. Recently, Carter et al. first succeeded in revealing the single crystal structure of HSA complexed with a hemin in its subdomain IB with a 1.9 Å resolution.[2] From the viewpoint of clinical application, dioxygen

 CCC 1022-1360/00/$ 17,50+.50/0